10

Ambient Bubble Acoustics: Seep, Rain, and Wave Noise

Ben Roche[1], Timothy G. Leighton[2], Paul R. White[2], and Jonathan M. Bull[1]

ABSTRACT

This chapter discusses the sounds emitted by gas bubbles when they are generated underwater. Here, we define bubbles to be volumes of gas surrounded by liquid (in this case, taken to be water), having surface-tension forces (the so-called *Laplace pressure*) generated by a single wall; they are distinguished from the soap bubbles familiar in children's games, where the volume of gas is surrounded by two gas/liquid boundaries. Compared to other acoustic sources, such as marine mammals, ships, and tectonic events, a single bubble may seem insignificant. Indeed, without ideal conditions, it can be difficult to observe the sound of a single bubble from a distance of more than a few tens of centimeters. However, natural processes rarely produce single bubbles and can generate them by the million, at which point the sound generated is significant. The formation of bubbles due to gas seeps, rainfall, and breaking waves is a major component of ambient noise in the marine environment and can even alter the propagation of sound waves from other sources. This chapter focuses on the passive emissions of bubbles as they are formed, released, or injected into water, with linear volume pulsations.

10.1. INTRODUCTION

In this chapter, we will discuss the mechanics behind an individual bubble's acoustic signature, particularly the Minnaert equation and other relevant properties, before discussing the formation of bubbles from subsurface gas migration, rainfall, and wave action, characterizing the acoustic nature of each process. The primary focus will be on the sound resulting from bubble generation from each source. Several different units are used to define each acoustic source; although this may appear confusing and make direct comparison difficult, we do this to be consistent with the literature. The topics covered here are broad, so the approach taken is to summarize the key principles and state of the field while providing substantial linkage to the literature.

[1]*School of Ocean and Earth Science, University of Southampton, Southampton, UK*

[2]*Institute of Sound and Vibration Research, University of Southampton, Southampton, UK*

10.2. BUBBLES AS ACOUSTIC SOURCES

Although bubbles may be found throughout the water column and produced in all manner of ways, from fish flatulence to volcanic emissions, it is only the initial formation of the bubble near the source that is of interest in passive acoustics. Additionally, only a few sources of bubble production are common and large enough to warrant a full discussion: bubbles released from gas seeps on the seabed and those produced by either rainfall or breaking waves at the surface. The following section will discuss the initial release of gas bubbles into a body of water and the resulting acoustic signal. These are the fundamental principles behind bubble acoustics and are directly applicable to all initial sources of bubble production.

Noisy Oceans: Monitoring Seismic and Acoustic Signals in the Marine Environment, Geophysical Monograph 284, First Edition. Edited by Gaye Bayrakci and Frauke Klingelhoefer.

DOI:10.1002/9781119750925.ch10

10.2.1. The Injection of a Gas Bubble

A bubble does not instantly appear fully formed in the water column. The gas is injected into the body of water over a very short time. Although there are several processes by which this injection can happen, the core principles remain the same: a small volume of gas from a larger reservoir encroaches into a body of water, with the two volumes of gas connected via a thin neck. As the small volume of gas extends further and further into the body of water, the neck is stretched thinner and thinner, eventually snapping and releasing the gas into the water as a distinct bubble. The snapping of the bubble neck is of most interest to us as it results in a jet of water being momentarily propelled into the bubble, triggering an initial volume oscillation. This volume oscillation ultimately results in the acoustic signal of a bubble release (Leighton, 1994; Longuet-Higgins et al., 1991; Czerski & Deane, 2010).

The easiest way to understand the process of bubble release is to study gas being injected into a body of water with a needle, as shown in Fig. 10.1. Theoretical calculations have been used to deduce the stages of bubble injection via a needle, reinforced by lab observations (Longuet-Higgins et al., 1991). These stages are best described in relation to the radius of curvature (the radius of a circular arc that best approximates the curve) of the meniscus at the top of the bubble; the scales are dimensionless. The bubble initially grows from the surface of the nozzle as gas flows through it, the radius of curvature decreasing from 1 to <0.5 with volume increasing steadily (t = –830 ms in Fig. 10.1). The bubble profile changes from nearly horizontal to semicircular in shape. Near the moment *the tangent to the meniscus at the point of attachment to the nozzle* becomes vertical (t = −730 ms in Fig. 10.1), the volume increases rapidly while the radius of curvature remains roughly constant (t = –480 ms in Fig. 10.1). Subsequently, the volume and radius of curvature increase steadily. Here, a neck begins to form; this is the narrowest part of the bubble profile, located between the nozzle and the main body of the bubble (t = –80 ms in Fig. 10.1). Once the radius of curvature equals ~0.655, the *tangent to the meniscus at the point of attachment* (now the neck of the bubble) becomes near vertical again, and there is a second sharp increase in volume. The bubble now has a distinct diapir-like shape (t = –2 ms in Fig. 10.1). The volume of gas in the bubble reaches a maximum; beyond this point, the bubble is considered unstable. Further air forced into the bubble causes it to detach, and the snapping of the neck releases it, allowing it to rise upward (t = 0 ms in Fig. 10.1). (Longuet-Higgins et al., 1991) The upper half of the neck recedes back into the bubble as a jet of water propels itself inward (t = 2 ms cross-section in Fig. 10.1); this decreases the volume of the bubble, resulting in a volume oscillation (Leighton, 1994; Longuet-Higgins et al., 1991; Czerski & Deane, 2010).

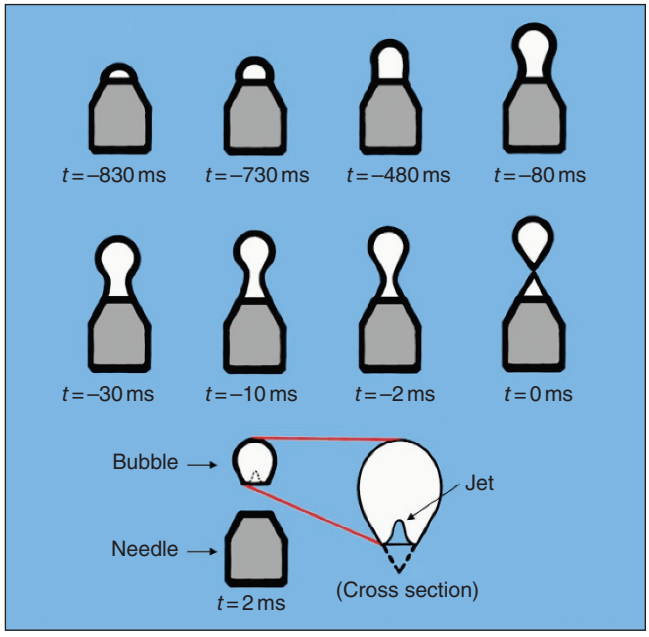

Figure 10.1 A bubble emerging from an underwater nozzle with internal diameter 4.00 mm. As the bubble grows, a neck forms between it and the injection nozzle; the neck eventually snaps, releasing the bubble and propelling a jet of water into it. This jet decreases the volume of the bubble and causes it to undergo simple harmonic motion. Times are given in milliseconds relative to the moment the bubble is detached (i.e., the neck snaps); note that these timings change with nozzle size and gas flow rate. Adapted from Longuet-Higgins et al. (1991) and Czerski and Deane (2010).

10.2.2. Bubbles as Simple Harmonic Oscillators

Immediately after its release into the water column, regardless of the means of production, a bubble begins to pulsate. The bubble itself may undergo a wide range of oscillatory changes in shape, but these can be decomposed into a summation of spherical harmonic pulsations; only one of these (the zeroth order) changes the bubble volume to first order and hence changes the gas pressure to first order (at low Mach numbers), and so couples to acoustic fields (Leighton, 1994). Therefore, even though the bubble often departs from sphericity, with a few notable exceptions that will not be discussed further in this chapter, it is appropriate when discussing the interaction with sound fields at low Mach numbers to refer to the pulsations of a spherical bubble. This oscillation approximates a simple harmonic oscillator at low amplitudes, occurring at the natural frequency of the bubble (Leighton, 1994). It is possible to derive the relationship between the radius of a bubble and the frequency of its

initial free oscillations by assuming there are no dissipative losses—for example, through viscosity or thermal conduction—via consideration of the flow between potential and internal energy. The natural frequency of bubble oscillation is known as the Minnaert frequency (Minnaert, 1933).

As a simple harmonic oscillator, the pulsation of a bubble is analogous to the classic bob on a spring system of unloaded length l_0 and loaded length l. The water around the bubble is the bob weight, and the gas within the bubble is the spring, as shown in Fig. 10.2a. Note that the water's contribution to the system's effective mass declines with distance from the bubble wall, so the mass is in effect finite. The displacement ε from the equilibrium position corresponds to displacement of the bubble wall R_ε between its equilibrium radius R_0 (the bob at $l - l_0$) and its present radius R at any given moment (the bob at $l + \varepsilon - l_0$), see Fig. 10.2. The gas pressure following compression or expansion restores the bubble to its equilibrium position, which is analogous to the spring stiffness in the spring–bob example. However, it is important to note that the gas in the bubble is less dense than the surrounding medium (unlike the bob in the air). So, whereas in the spring–bob system, inertia and momentum are dominated by the bob, the inertia of the water surrounding a bubble dominates in the bubble system, the mass of the gas being negligible.

This final stage of the bubble formation triggers the simple harmonic motion of a bubble (Leighton, 1994; Czerski & Deane, 2010). The neck snapping triggers an initial volume oscillation that acts as an exciting force, causing the bubble to emit sound at its natural frequency. We assume this initial driving impulse is of infinitesimally small duration, meaning that while the bubble undergoes subsequent oscillation, it effectively experiences no driving force.

With this idea of a bubble as a simple harmonic oscillator, we can describe the shape of the bubble over time. Imagine a bubble (Fig. 10.2b) with a mean radius R_0 that remains spherical at all times while undergoing a volume oscillation at a frequency ω_0. The expressed maximum displacement of the bubble wall is $R_{\varepsilon 0}$ so that $R_{\max} = R_0 + R_{\varepsilon 0}$ and $R_{\min} = R_0 - R_{\varepsilon 0}$. Thus the bubble radius R at any time t can be expressed as the real part of

$$R = R_0 + R_\varepsilon(t) = R_0 + R_{\varepsilon 0} e^{i\omega_0 t}. \tag{10.1}$$

The displacement of the bubble wall R_ε from equilibrium over time describes a motion

$$R_\varepsilon = -R_{\varepsilon 0} e^{i\omega_0 t}. \tag{10.2}$$

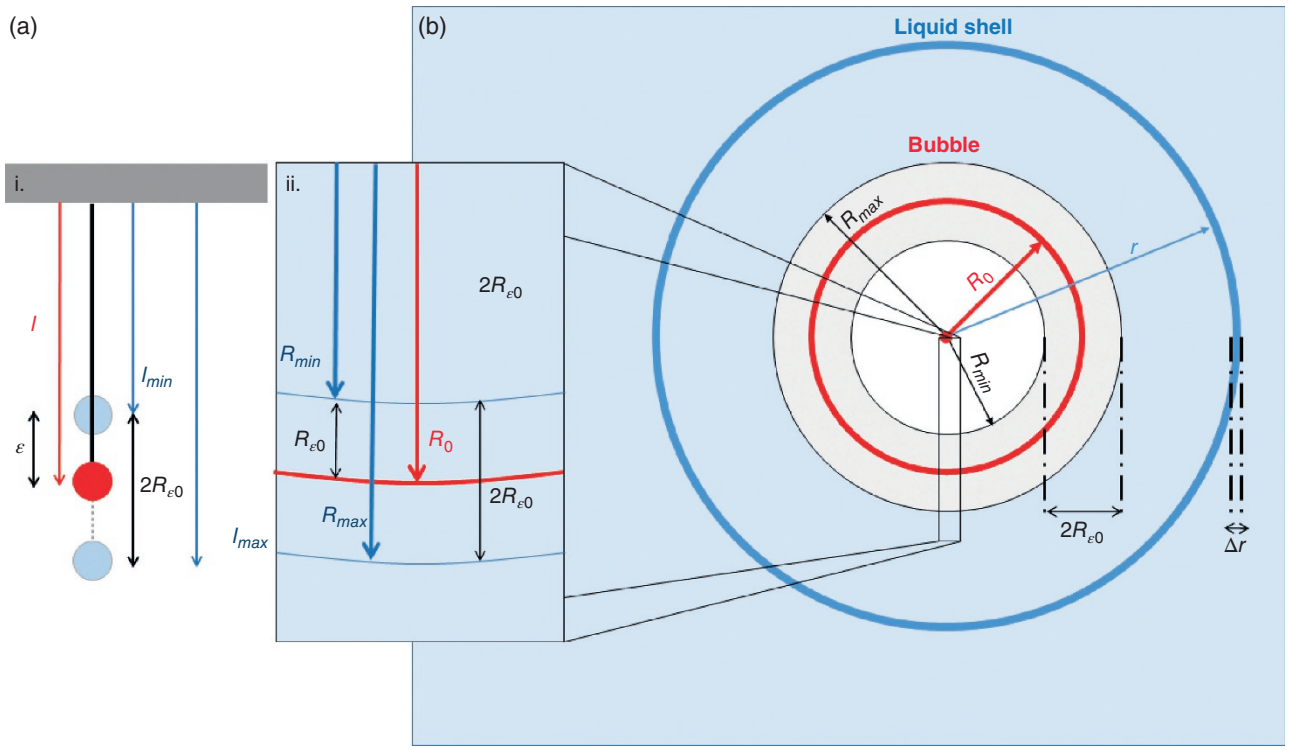

Figure 10.2 (a) Diagram comparing simple harmonic oscillators i. A spring bob system. ii. A bubble wall moving. (b) Diagram of a bubble of radius R_0, the wall of which is undergoing small-amplitude oscillations of amplitude $R_{\varepsilon 0}$. It is surrounded by spherical shells of liquid, one of which has a radius of r and a thickness of Δr.

10.2.3. Minnaert Frequency

With a description of the motion of the bubble wall over time, we can describe the flow between kinetic and potential energy. From here, we can apply the concept to the conservation of energy to derive the Minnaert (or natural) frequency of a bubble (Leighton, 1994; Minnaert, 1933):

$$f_M = \frac{1}{2\pi R_0}\sqrt{\frac{3\kappa p_0}{\rho}}, \tag{10.3}$$

where ρ is the density of water, p_0 is the hydrostatic liquid pressure outside the bubble, and κ is the polytropic index (which takes a value equal to unity when the gas behaves isothermally and equals the ratio of the specific heats of the gas at constant pressure to that at constant volume when the gas behaves adiabatically). A full derivation of the Minnaert frequency can be found in the appendix of this chapter.

The Minnaert equation demonstrates that the frequency of a bubble's oscillation is inversely proportional to its equilibrium radius R_0. As the other factors are fairly consistent or easily predictable (polytropic constant, density of water, water pressure outside the bubble), it is relatively easy to measure the size of a bubble based on its acoustic signal. As a general rule of thumb for bubbles near the surface, the radius in millimeters multiplied by the frequency in kilohertz is equal to approximately 3: that is, a 1 mm radius bubble has a 3 kHz frequency, a 1.5 mm radius bubble has a 2 kHz frequency, and a 3 mm radius bubble has a frequency of 1 kHz.

Once a bubble starts oscillating, it begins to lose energy in three ways. (1) Most importantly for us, energy is radiated from the bubble through acoustic waves (radiation damping). (2) Energy is lost through conduction between the gas and the surrounding liquid (thermal damping). (3) Energy is lost moving the water around the bubble as it oscillates (viscous damping) (Leighton, 1994). Because of these factors, the bubble can be considered lightly damped (Ainslie & Leighton, 2011). This damping is typically described by the quality factor of the bubble, Q, which is approximately defined as the ratio of the initial energy to the energy lost in one radian cycle of oscillation (Walton et al., 2005). We will avoid a full discussion of the damping constant of a bubble (see Ainslie and Leighton [2011] for this) and note that the oscillation of millimeter-sized bubbles decays exponentially over ~10–30 milliseconds (Leighton, 1994) and varies with gas content: that is, for air bubbles, $Q = 34$; for pure methane bubbles and carbon dioxide bubbles, $Q = 24$ and 29, respectively (Walton et al., 2005).

The polytropic adaptation of the Minnaert equation was first used in the 1980s to infer the size distribution and number of bubbles formed in the natural world in waterfalls and streams (Leighton & Walton, 1987). In subsequent years, this method was extended to do the same for bubbles entrained by breaking waves (Medwin & Beaky, 1989) and rainfall (Pumphrey & Crum, 1990). It works well when the signature passive emission from each bubble is clearly separated in time from others; however, this method of counting and sizing bubbles becomes more difficult as the signatures from each bubble get closer in time and overlap. Although signal-processing techniques can alleviate the problem (Leighton et al., 1998), eventually the degree of overlap becomes so great that this technique must be replaced by a spectral approach (discussed later) (Leighton & White, 2012).

A recording of a bubble signature (Fig. 10.3) shows a sinusoidal wave that decays exponentially, indicative of a lightly damped oscillator with a frequency consistent with that predicted by the Minnaert equation (equation 10.3). Note that because the sound generated by a bubble is an exponentially decaying sinusoid, the sound contains a range of frequencies, and the spectral profile of each bubble is Lorentzian (Leighton, 1988), centered around the natural frequency (Leighton, 1994). The bubble in Fig. 10.3 was released at a water depth of 2.5 m and has a frequency of 0.38 kHz. Using equation 10.3 (or the rule of thumb $R_{0(\mathrm{mm})} = 3/f_{M(\mathrm{kHz})}$), this corresponds to a radius of 7.9 mm.

The Minnaert equation was later adapted to include the effects of vapor pressure p_v, surface tension σ, and shear viscosity η and so is more correctly presented as (Leighton, 1994, 2004)

$$f_M = \frac{1}{2\pi R_0\sqrt{\rho_0}}\sqrt{3\kappa\left(p_0 - p_v + \frac{2\sigma}{R_0}\right) - \frac{2\sigma}{R_0} + p_v - \frac{4\eta^2}{\rho_0 R_0^2}}. \tag{10.4}$$

Figure 10.4 shows the natural frequency of bubbles calculated using equation 10.4 at various sizes and depths.

Bubbles generated near the ocean surface have a natural frequency f_0, which is slightly higher than that specified by the Minnaert equation due to the reduced inertia of the fluid near the surface. A similar effect occurs if the water surrounding the bubble also contains bubbles in close proximity. Strasberg (1953) calculated the effect on the frequency, showing that

$$f_0 = \frac{f_M}{\sqrt{1 - (R_0/2h) - (R_0/2h)^4}}, \tag{10.5}$$

where h is the distance from the *center* of the bubble to the surface of the water. As h is always greater than R_0, the denominator is always less than 1, so the oscillation of a bubble in the near surface is always slightly greater than that predicted by the Minnaert equation. For example, a bubble at depth $h = 4R_0$ has a frequency ~7% higher. Alternatively, one should also be able to see that when

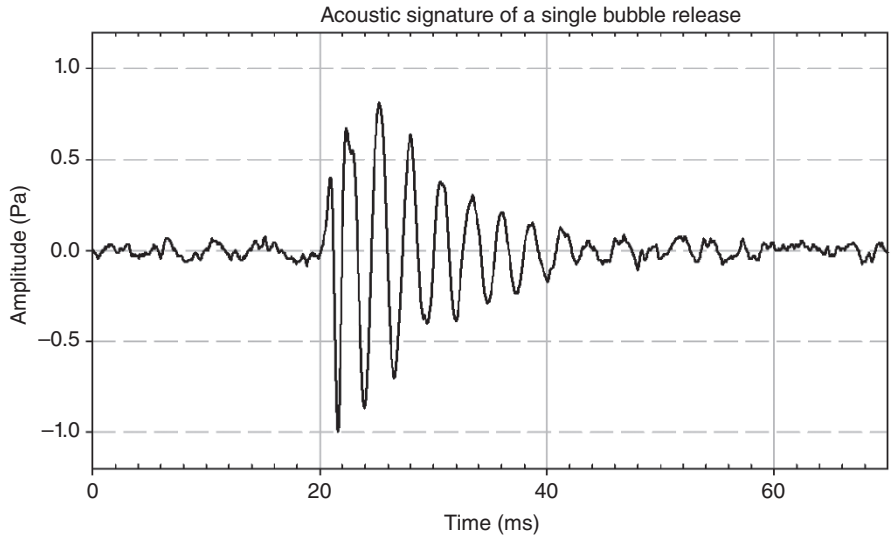

Figure 10.3 Sonogram displaying the typical acoustic emission of a bubble as recorded by a hydrophone. The bubble was released from sediment at a water depth of 2.5 m, 25 cm from the hydrophone. It became detached at around 20 ms, triggering simple harmonic oscillation resulting in an exponentially decaying sinusoidal wave. The bubble oscillates with a frequency of 0.38 kHz (t = 2.6 ms), which we can invert via the Minnaert equation (equation 10.3) to indicate a radius of 7.9 mm.

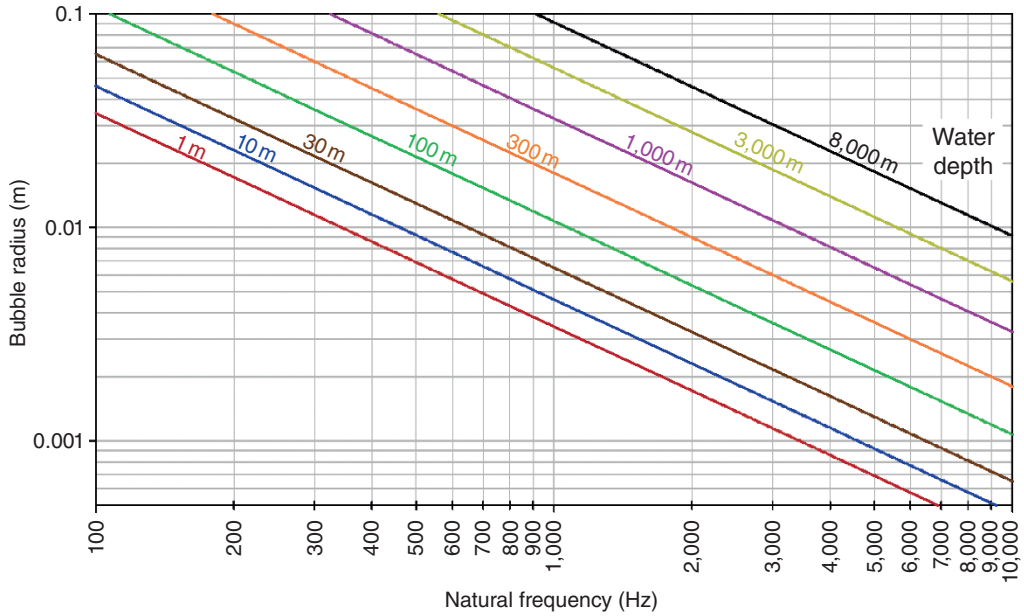

Figure 10.4 Graph displaying the natural frequency of bubbles of various sizes according to the refined Minnaert in equation 10.4 at a range of water depths (1, 10, 30, 100, 300, 1,000, 3,000, and 8,000 m). Calculated assuming ρ = 1,000 kg/m^3 and κ = 1.4 at a temperature of 10 °C and a salinity of 0%.

$h \gg R_0$—that is, the bubble is a few tens of centimeters or more beneath the water's surface—the frequency of the bubble is equal to the Minnaert frequency:

$$f_0 = f_M \text{ for } h \gg R_0. \tag{10.6}$$

Another notable deviation from the Minnaert equation occurs when bubbles are generated (nearly) simultaneously in close proximity, as is the case with wave-generated bubbles. The bubbles are linked by acoustic and hydrodynamic interactions, resulting in coupled oscillator systems that tend to oscillate at much lower frequencies than the natural frequency of any individual bubble within the system. In effect, a cloud of small bubbles can emit an acoustic signature similar to that of a much larger bubble. A region of

bubbly water containing a total of N_b identical bubbles (each having a radius R_0 and a natural frequency of f_0) forms an air–water mixture with a void fraction VF. If this bubbly water is submerged in bubble-free water and the boundary between the two is assumed to be rigid (a poor assumption but a useful starting point), the modal frequency f_n of a bubble cloud can be given by (Lu et al., 1990)

$$f_n = f_0 \frac{n}{N_b^{1/3} \cdot \{VF\}^{1/6}}, \tag{10.7}$$

where n is the mode of oscillation. It should be apparent that for any cloud with more than a few hundred bubbles, the lower-order modal frequencies will be lower than the natural frequency of the individual bubbles. For example, a 10 cm cloud of 1,000 bubbles will have a first-order modal frequency one-third that of the bubble oscillations (Leighton, 1994). The greater the number of bubbles in the same space, the lower the modal frequency. Obviously, bubble clouds do not have rigid walls, but the general trend holds true, with complexities in cloud geometry and bubble-size distribution being a greater source of error. In practice, this means if bubbles exist in clouds, the emission—and, perhaps more prominently, the scattering—of sound by the cloud of bubbles contains elements at this cloud frequency, in addition to the signals of the individual bubble resonances (Leighton, 1994).

In summary, releasing a bubble into the water column causes it to undergo simple harmonic oscillation. The resulting acoustic signal is an exponentially decaying sinusoidal wave at the natural (or Minnaert) frequency of the bubble, which is approximately inversely proportional to its equilibrium radius. Measuring the volume of gas release at slow sources of bubble production (a few hertz) acoustically is relatively trivial. One simply needs appropriate recording equipment and an understanding of the basic field or lab conditions (water depth, etc.) to individually count and size each bubble signal without knowing the energy emission from an individual bubble (Leighton & White, 2012). Indeed, this signature method of flux measurement can even be used as an undergraduate lab experiment. However, as we will discuss later, measuring the volume of released gas becomes increasingly difficult as the rate of bubble production increases.

10.3. SUBSURFACE GAS RELEASE

Gas can be generated below the seabed from several sources: thermogenic, biogenic, and anthropogenic. When this gas reaches the seabed, it escapes upward into the water column by the formation of bubbles (Judd, 2003; Knittel & Boetius, 2009; McGinnis et al., 2006). This can have a major impact on ocean chemistry via dissolution and is a poorly understood part of the global carbon cycle (Roche et al., 2020; Johnson et al., 2012; Johnson et al., 2002; Jain & Juanes, 2009). Additionally, the release of each bubble produces an acoustic signal, which can affect the soundscape in local areas (Leighton, 1994; Leighton & White, 2012; Maksimov et al., 2016). The sound is emitted as soon the bubble detaches from the seafloor and lasts ~20 ms, which, given that bubbles tend to rise upward at a speed of 20–30 cm/s, confines the production to within ~5 mm of the seafloor. We will first describe the passage and release of a single bubble before discussing localized seeps, their resultant signal, and flux inversion techniques. The following applies to bubbles of any gas type, with the Minnaert frequency varying only slightly as described by equation 10.4.

In a typical near-surface marine sediment, the pores between grains are saturated with water. If gas is introduced, such as from an underlying fault, it slowly invades the surrounding pores, displacing the water. This intrusion can occur either by capillary invasion or fracture opening (Johnson et al., 2012; Johnson et al., 2002; Jain & Juanes, 2009). The difference in density between the gas and the surrounding medium creates a buoyancy force, which typically causes the gas to rise upward (Algar et al., 2011; Boudreau et al., 2005; Boudreau, 2012). When the gas reaches the seabed, it continues to rise due to buoyancy forces. The sediment pores act like a kind of nozzle, akin to a needle in a test tank, through which the bubble is injected into the water column (Leighton & White, 2012; Roche et al., 2020). The bubble escapes into the overlying water when the buoyancy forces acting on it overcome the adhesive-like forces attaching it to the sediment.

The passage of gas through the upper few centimeters of the seabed can cause a weak oscillatory signal, audible in the water column, possibly as the grains rearrange to create an orifice for the bubble beneath the surface (Leighton, 1994). Vazquez et al. (2015) observed this event using synchronous high-speed video and acoustic recordings of gas migrating through granular sediment. The signal appears unpredictable and is expected to vary with grain size, grain type, bubble size, water pressure, etc. Indeed, some experimental evidence indicates that the sound is absent for fine silts and coarse pebbles. As the magnitude of this precursor signal is smaller than that of subsequent bubble oscillation, the phenomenon remains largely unexplored. Thus, the acoustic signature of a single bubble released from sediment can be defined as an exponentially decaying sinusoidal wave resulting from bubble oscillation (Leighton & Walton, 1987), potentially preceded by a weak, unpredictable oscillatory signal in certain sediment types (Vazquez et al., 2015), as shown in Fig. 10.5.

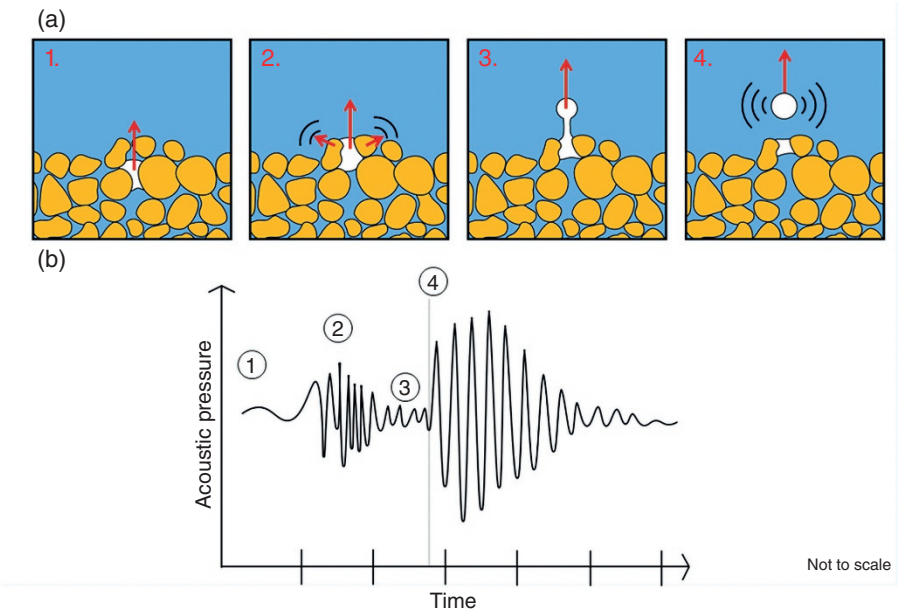

Figure 10.5 (a) The release of a bubble from granular sediment. (b) The corresponding acoustic signal. Note (2) the chaotic weak signal resulting from the rearrangement of grains as the gas reaches the seabed and (4) the stronger distinct acoustic signature of the bubble being released into the water column. Adapted from Vazquez et al. (2015).

10.3.1. Gas-Seep Acoustics

The continuous passage of gas through the same area may cause the development of open channels (or chimneys) in the sediment, which direct the flow of gas to a single localized point on the seabed, forming a seep (Suess, 2014; Coughlan, et al., 2021; Hovland, 2002). A *subsea gas seep* is broadly defined as the *continuous* release of gas from the seabed into the water column. There is no set magnitude for the flux of gas from a seep (Suess, 2014; Coughlan, et al., 2021; Hovland, 2002), meaning the term encompasses seeps that release tens to millions of bubbles per minute. Similarly, there are no strictly defined time scales for being continuous; some seeps are born and die within a few hours, some are only active for certain times of the day or year, and others have been active for centuries (Coughlan et al., 2021; Li et al., 2020b; Böttner et al., 2019). It is also worth noting that a seep does not have to be in sediment; it may also come from exposed bedrock or even manmade features such as leaking pipes. The term *pockmark* is often synonymous with gas seeping from sediment, although strictly speaking, the term only defines the depressions created in the seabed by the gas release (Coughlan et al., 2021; Böttner et al., 2019).

The size of a bubble released from the seabed is difficult to predict. In a lab, the size of a bubble released from a needle is generally considered a factor of the size of the nozzle, the gas injection pressure, and the overlying water pressure, although even these have limited control of bubble size (Longuet-Higgins et al., 1991; Leighton et al., 1991). Even in a controlled setting, it is difficult to regularly produce identically sized bubbles, making bubble size highly variable in the field. Assuming the pores between grains act as nozzles, one might anticipate that larger pore spacings, which are generally associated with larger and more rounded grains, would generate larger bubbles. However, when open conduits form in sediment, pore size becomes less important than conduit size, which can vary significantly based on numerous factors, including the chimney's age. Consequently, bubble-size distributions are unique for each seep. Indeed, the exact bubble-size distribution (and thus gas flux) is likely to change over time as the underlying conduits evolve and the overlying water pressure fluctuates with tidal and seasonal variations (Römer et al., 2016; Bergès et al., 2015; Sultan et al., 2020; Boles et al., 2001; Scandella et al., 2016; Klaucke et al., 2010; Riedel et al., 2018; Leifer, 2015; Wiggins et cl., 2015). Gas flux from underwater seeps can also vary due to underlying causes such as seabed temperature and seismic or volcanic activity (Leifer, 2015; Leifer & Patro, 2002; Muyakshin & Sauter, 2010; Ostrovsky et al., 2008; Li et al., 2020a; Esposito et al., 2006). In deep marine settings, bubble sizes have commonly been observed between 1 and 6 mm in radius (Bergès et al., 2015; Li et al., 2020a); shallower waters (<10 m) have been observed to contain larger bubbles greater than 10 mm in radius (Leighton, 1994; Leighton & White,

2012; Li et al., 2020b; Li et al., 2021), although this trend is far from a rule and exceptions are plentiful.

The acoustic signature of a seep is thus defined by its bubble-generation rate: the rate at which bubbles of different sizes are released. Unfortunately, as every seep has a unique bubble-generation rate, it is difficult to define a general rule for passive acoustic emissions. In the simplest case of a slow seep releasing a few bubbles per second, its acoustic emission can be defined by the continuous release of bubbles: a continuous repetition of the signal seen in Fig. 10.3 (Leighton & White, 2012; Greene & Wilson, 2012). Ultimately, these signals are weak and have little impact on the marine soundscape due to the low flux rates, meaning they are of little interest to many researchers.

Larger seeps with higher gas-flux rates generate stronger signals, which can be observed at greater distances and may have a noticeable impact on ocean chemistry. However, as the frequency of bubble release increases with flux rate, eventually the acoustic signals of each release begin to overlap, making it impossible to distinguish individual bubble oscillations (Bergès et al., 2015; Roche et al., 2019; Chen et al., 2016).

By considering the combined signal of multiple bubble releases, Leighton and White (2012) derived the power spectral density $S(\omega)$ of the far-field acoustic signature of a gas seep at some distance r:

$$S(\omega) = \int_0^\infty B(R_0)|X_b(\omega, R_0)|^2 dR_0, \tag{10.8}$$

where ω is the angular frequency and $B(R_0)$ is the bubble-size distribution as a function of R_0 defined such that $\Psi(n) = \int_{R_1}^{R_2} B(R_0)dR_0$ represents the number of bubbles generated per second with a radius between R_1 and R_2: that is, the bubble generation rate, δ_{tot}, is the total damping constant for pulsation at resonance, and

$$|X_b(\omega, R_0)|^2 = R_{\epsilon 0i}^2 \frac{\omega_0^4 R_0^4 \rho^2}{r^2} \left(\frac{4\left[(\omega_0\delta_{tot})^2 + 4\omega^2\right]}{\left[(\omega_0\delta_{tot})^2 + 4(\omega_0 - \omega)^2\right]\left[(\omega_0\delta_{tot})^2 + 4(\omega_0 + \omega)^2\right]} \right). \tag{10.9}$$

The important unknown in this equation is the initial amplitude of displacement of the bubble wall at the start of the emission ($R_{\epsilon 0i}$) (not to be confused with $R_{\epsilon 0}$ the maximum displacement of bubble wall from the equilibrium radius). There is strong evidence to suggest this is a function of the equilibrium bubble radius (R_0). However, this exact relationship is yet to be defined. Consequently, many studies have elected to treat $R_{\epsilon 0i}/R_0$ as a constant somewhere between 1.4×10^{-4} and 5.6×10^{-4}, based on experimental observations (Leighton & White, 2012. However, it should be stressed that this is a pragmatic choice with no theoretical foundation. It is important to note that the above formulation excludes the signal from the rearrangement of grains before a bubbles release. However, this is reasonable because (1) the signal is very weak (Vazquez et al., 2015), and (2) seeps with a higher flux contain open conduits that do not require grains to be rearranged to facilitate the migration of gas (Roche et al., 2020).

This spectral approach allowed Leighton and White to invert the signal from a given gas seep (at a known distance from a hydrophone) to determine the number of bubbles of various sizes released within a given period, providing them with an estimate of gas flux (Leighton & White, 2012). In replacing the signature method for counting and sizing bubbles in circumstances where their passive acoustic emissions overlapped, Leighton and White drew particular attention to the lack of knowledge about the energy of an individual bubble's emission. Although the signature method had managed to bypass this unknown, their spectral method could not. Although the spectral method had the power to count and size bubbles when the signatures overlapped, Leighton and White noted that the reliance on literature values for the energy released by a bubble was the greatest source of uncertainty, particularly as the energy associated with the release of a given bubble is likely to vary with the mode by which it is entrained (injected by a needle, through sediment, via a gas pipe leak, or entrained in the upper ocean by rainfall or breaking waves) and the depth at which it is entrained. In simple terms, if the count of bubbles of a certain size is based on the energy detected in a given frequency band, then if the acoustic energy in that band is divided between the bubbles contributing to it, the estimation calculates fewer bubbles entrained, the more acoustic energy is contained in each bubble signature (Leighton & White, 2012). Further complications were identified in that a given injection process can cause a bubble to fragment after release or merge with other bubbles, which can lead to the injection of a single bubble generating multiple signatures (Leighton et al., 1991). Despite all this, the use of the spectral method in the field has proven effective to date, providing continuous estimates of gas flux over extended periods as validated by intermittent physical measurements. However, a need to reduce the uncertainty in these measurements is continually noted (Bergès et al., 2015; Li et al., 2021; Roche et al., 2019).

Given the highly variable nature of seafloor gas seeps, particularly regarding the size of the bubbles and their rate of release, it is difficult to give a general impression of

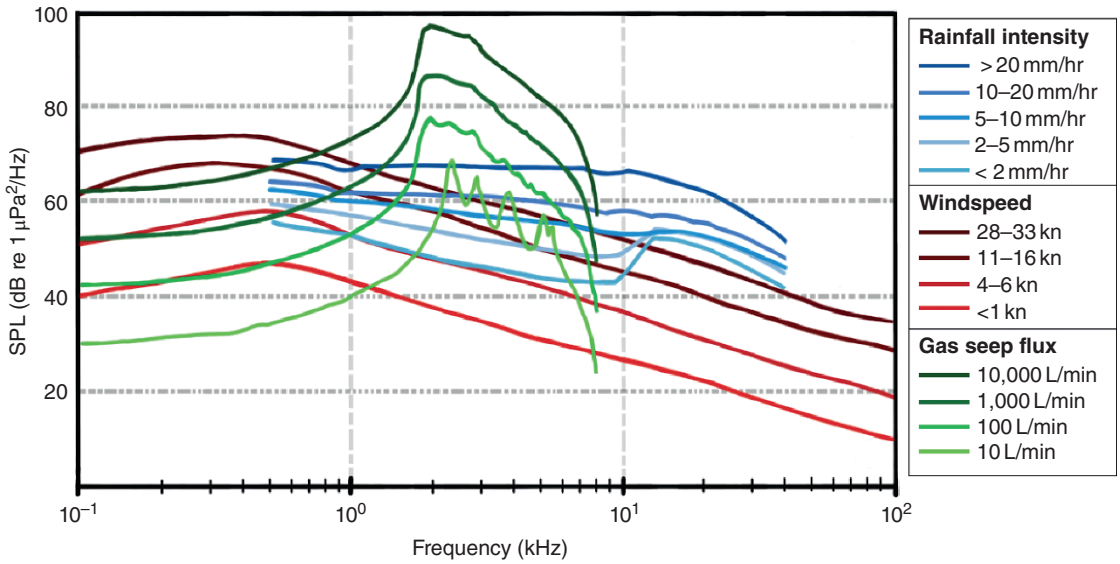

Figure 10.6 Ambient noise spectral density from 0.1 to 100 kHz for common bubble-production sources in the marine environment, including gas seeps, rainfall, and breaking waves. Gas seepage is simulated at different flux rates in L/min at 100 m water depth, assuming a Gaussian bubble size distribution with radius between 0.5 and 10 mm. Rainfall data at different intensity levels in mm/hr is from Ma and Nystuen (2004), and breaking wave data observations at different wind speeds in knots is from Wenz (1962).

their contribution to the marine soundscape. To do so here, we use the above equations to simulate the sound pressure level (SPL) of a single point-focused seep venting gas at the rate of 10, 100, 1,000, and 10,000 L/min, assuming a log-normal bubble-size distribution with radius between 0.5 and 10 mm. The results are displayed in Fig. 10.6 alongside the SPL of various intensities of wind- and rain-generated bubble noise. We emphasize that these graphs are meant to serve only as an approximate guide to the potential effect natural seeps can have on the marine soundscape. Here, we see that the signal is confined mainly between 1 to 10 kHz (a result of the selected bubble-size distribution), with the magnitude of the signal increasing in line with the rate of gas flux. A maximum amplitude of 97 dB re 1 $\mu Pa^2/Hz$ is seen at 10,000 L/min, well in excess of wind- and rain-generated bubble noise.

In summary, the release of gas from the seabed generates an acoustic signal at the natural frequency of the resulting bubble. As the gas flow out of a seep increases, the acoustic signals of each bubble released begin to overlap, making the resultant signal a summation of each individual bubble's natural frequency. Consequently, it is currently impossible to predict the sound resulting from a gas seep (or a field of seeps) without understanding the bubble-size distribution. However, by observing the acoustic signature of a known seep, it is possible to quantify the size of bubbles being released and thus estimate the flux, observing tidal and seasonal variations.

10.4. RAINFALL ACOUSTICS

When a rain droplet impacts a body of water, it forms an impact crater and may entrain a bubble (Fig. 10.7). Consequently, falling rain produces two sounds in the marine environment: (1) the initial impact of the droplet on the body of water, which generates a compressional wave; and (2) the simple harmonic motion of a bubble following its release into the water, once again at the Minnaert frequency (Leighton, 1994). This scenario is directly comparable to a leaky tap dripping water into a sink, producing a distinct "plinking" noise (Leighton, 1994; Pumphrey & Elmore, 1990; Pumphrey & Walton, 1988). Although some incorrectly assume that this sound is a consequence of the initial collision between the drop and the water surface, the entrainment of bubbles produces the majority of the acoustic signature. We will first discuss the sound of the initial droplet impact before discussing the processes of entrainment, the resulting acoustic signature of rainfall, and methods of rainfall quantification.

The impact of the rain droplet on the water's surface initially produces a sharp acoustic pulse with a duration of 10–40 μs, as a result of the water-hammer effect (a pressure surge caused when the motion of a fluid is stopped). The pressure radiated by the impact is given by Pumphrey & Crym, 1990)

$$p_{\text{impact}} = \frac{\rho u_d^3 L_d}{2c} \frac{\cos\theta}{r} u, \qquad (10.10)$$

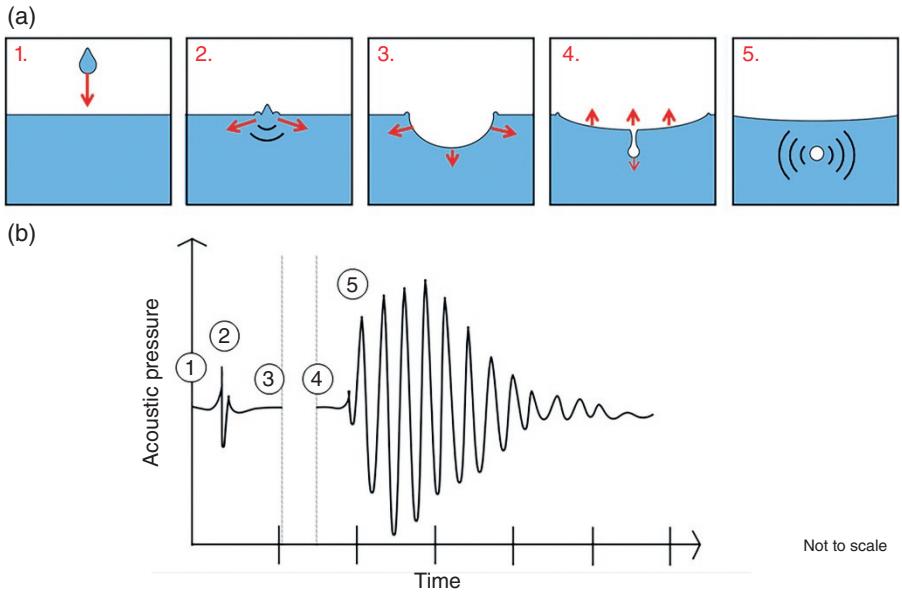

Figure 10.7 (a) A diagram of regular entrainment of a bubble following the impact of a water droplet. (b) The acoustic signature of a raindrop. Note the weak, sharp signal from the impact (2) followed by the larger oscillation of the bubble (5) once it detaches from the crater. Adapted from Medwin and Nystuen (1990).

where ρ is the water density, u_d is the impact speed of the droplet, L_d is the diameter of the droplet, c is the speed of sound in water, θ is the angle between the observer and sound source relative to the z axis, and u is the impact Mach number. Raindrops typically have a diameter between 0.5 and 5.0 mm (larger droplets tending to break up), resulting in an impact velocity between ~2.0 and 9.0 m/s (Nystuen, 2001). This means that although for individual droplets, it is easy to identify the impact signature, this sound is dwarfed by the later oscillation of a bubble by a factor as large as 200:1. During rainfall (where bubbles are continuously oscillating), the sound of impact has very little effect on the overall acoustic signature and is responsible only for a weak broadband signal (Pumphrey & Elmore, 1990).

The entrainment of a bubble by a droplet of water is a dynamic process, much more complex than the injection of gas through sediment pores. The exact mechanism by which this occurs varies based on several factors, mainly impact velocity and droplet diameter. These processes are (Pumphrey & Elmore, 1990) as follows:

1. *Irregular entrainment:* The complex and unpredictable details of a splash somehow entrain a bubble(s).
2. *Regular entrainment:* A retreating impact crater leaves behind a small volume of gas connected via a narrow neck that is eventually pinched off, leaving behind a single bubble (see Fig. 10.7a).
3. *Entrainment of large bubbles:* Most of the volume of the crater is trapped as a bubble.
4. *Mesler entrainment:* Many tiny bubbles are trapped in the early stages of the impact process, possibly between the crest of capillary waves on the droplet and body of water.

Bubbles produced by entrainment act identically to examples discussed previously, oscillating to produce an exponentially decaying sinusoidal wave in the near field (Pumphrey & Elmore, 1990). The only notable difference from seabed gas release is that the bubbles are much closer to a free surface (the water surface), meaning the mass of water regulating the oscillations is lower, and thus the natural frequency of the bubbles is slightly higher than the Minnaert frequency (see equation 10.5).

Given a large enough area and a sufficient number of raindrops (of a consistent size distribution), one can assume that a constant number of raindrops are impacting the water per second, and therefore a constant number of bubbles are being entrained. Consequently, rainfall results in a constant ambient noise. Using this principle, and quantifying the number of bubbles entrained per second $n(f)$ in a 1 Hz frequency band over a 1 m^2 area of water, Pumphrey and Elmore (1990) were able to show that the intensity below the surface of the oscillating bubbles at any given frequency f is

$$I_{\text{Rain}} = \frac{n(f)D^2Q}{4f\rho c}, \tag{10.11}$$

where Q is the quality factor and D is the initial dipole strength of the bubble. From this, the intensity spectrum level is given by

$$ISL_{\text{Rain}} = 10\log\frac{I_{\text{Rain}}\cdot\rho c}{1\ \mu\text{Pa}^2/\text{Hz}} = 10\log\frac{n(f)D^2Q/4f}{1\ \mu\text{Pa}^2/\text{Hz}}. \tag{10.12}$$

It is important to note that whereas D increases with increasing f, Q decreases. these two effects cancel each other out, so the spectrum is dominated by the number of bubbles entrained per second (Pumphrey & Elmore, 1990). Additionally, it has been observed that, neglecting refraction and absorption, 90% of the rain signal arrives from a sample area with a radius equal to three times the observer's depth (Pumphrey & Elmore, 1990). Thus, using equation 10.12 and the size and number of bubbles produced per second by entrainment, one can calculate the acoustic spectrum produced by rainfall or vice versa.

It is difficult to precisely predict the relative occurrence of each entrainment process during a rainstorm. Although regular entrainment is by far the most well-understood process, its name is primarily a consequence of being the easiest to comprehend and predict. Indeed, when Pumphrey and Elmore (1990) mapped which process occurs at which ratio of impact velocity to drop diameter, the plot is dominated by Mesler entrainment. Additionally, if one were to assume all impacts occurred at terminal velocity, the entrainment of large bubbles would never occur, and irregular entrainment would occur only during storms with particularly large droplets (Pumphrey & Elmore, 1990; Nystuen, 2001; Ma & Nystuen, 2005; Black et al., 1997; Serra, 2018; Yang et al., 2015; Pensieri et al., 2015; Taylor et al., 2020; Nystuen et al., 2015; Ashokan et al., 2015; Anagnostou et al., 2008; Nystuen et al., 2008). It is logical to assume that the splashing of water will produce some droplets that impact below terminal velocity, meaning all entrainment processes are likely to occur at some point during a rainstorm. However, it is reasonable for now to assume only regular and Mesler entrainment dominate and justify further consideration.

Mesler entrainment produces multiple very small bubbles ~25 μm in radius regardless of the size and velocity of the droplet. This results in a natural frequency of approximately 1.3 MHz. The high frequency and small size of Mesler bubbles ultimately means they produce very little noise, with high levels of attenuation. Consequently, they have little to no impact on the acoustic signature of rainfall, especially in the far field, and thus regular entrainment is responsible for the majority of bubble-oscillation sound during rainfall (Pumphrey & Elmore, 1990; Nystuen, 1986, 2001; Ma & Nystuen, 2005; Black et al., 1997; Serra, 2018; Yang et al., 2015; Pensieri et al., 2015; Taylor et al., 2020; Nystuen et al., 2000, 2015; Ashokan et al., 2015; Scrimger et al., 1987; Pumphrey, 1989; Nystuen & Selsor, 1997).

Regular entrainment produces different bubble sizes for different droplet sizes and impact velocities. If we consider only the bubbles produced by raindrops traveling at terminal velocity, regular entrainment is the result of droplets 0.40 to 0.55 mm in radius (with larger and smaller droplets resulting in Mesler entrainment) (Ma & Nystuen, 2005; Ashokan et al., 2015; Nystuen et al., 2000). Bubbles produced by regular entrainment of droplets of this size are predicted to be in the range of 0.16 to 0.33 mm in radius, resulting in frequencies between 10 and 20 kHz. Laboratory and field data has consistently shown a general increase in the number of bubbles entrained with bubble radius, peaking at ~0.23 mm in radius and dropping off rapidly above ~0.27 mm (Pumphrey & Elmore, 1990; Ma & Nystuen, 2005; Pensieri et al., 2015; Ashokan et al., 2015; Nystuen et al., 2008).

Consequently, the spectral content of rainfall on a body of water is expected to gradually increase in intensity with decreasing frequency, leading to a large peak at around 14–15 kHz followed by a sharp decline below 10–12 kHz. The exact intensity of the signal depends on the number of bubbles entrained per second (a consequence of the number of raindrops impacting per second) (Nystuen, 2001; Ma & Nystuen, 2005; Ashokan et al., 2015). This prediction fits well with field observations (see Fig. 10.8). Data collected from lakes, land-based water tanks, brackish ponds, and deep marine environments all show a distinctive peak at 14–15 kHz with a sudden drop-off below 10–12 kHz (Nystuen, 2001).

One consistent observation in repeat studies is a decrease in the prominence of the 14–15 kHz peak with increased rates of rainfall, with the peak being almost indistinguishable above 30 mm/hr (see Figs. 10.6 and 10.8) (Medwin et al., 1990; Ma & Nystuen, 2007). This

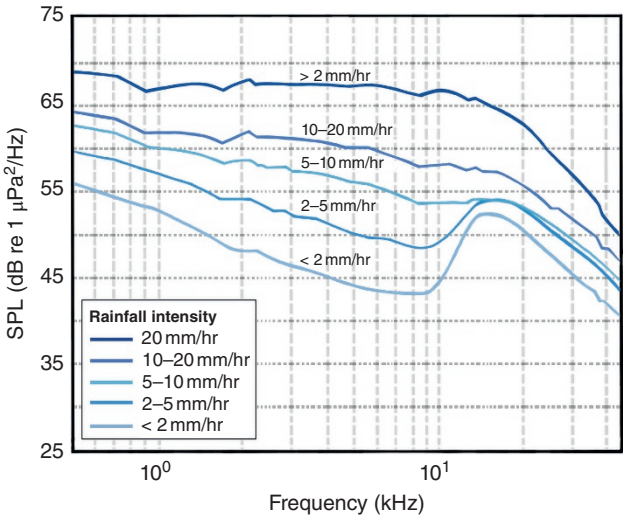

Figure 10.8 The average SPL spectra of rainfall acoustic signals at various rates as recorded by buoys in lakes and seas worldwide over a collective total of 30 months. Note the distinct peak at 14 kHz caused by the regular entertainment of bubbles from rainfall that becomes less prominent as rainfall becomes more intense. Adapted from Ma and Nystuen (2004).

is because at higher rainfall rates, more bubbles oscillating between 10 and 20 kHz are generated per second, resulting in increased signal intensity. However, as can be seen in equation 10.12, this is a logarithmic increase with diminishing returns: although the surrounding frequencies increase in intensity, the 14–15 kHz peak is relatively unmoved, flattening the spectrum. Additionally, in the field, increased rainfall tends to be accompanied by increased windspeed, which, as discussed next, also affects the rain spectrum. For this reason, the rain spectrum is best observed during a drizzle or light rain (Cavaleri & Bertotti, 2018).

The rain signature above 10 kHz is known to be affected by wind speed (Pumphrey & Elmore, 1990; Ma & Nystuen, 2005; Black et al., 1997; Anagnostou et al., 2008). Ma and Nystuen (2004) noted that as wind speed increased from 0.6 to 3.3 m/s, the 15 kHz peak became less prominent and broader, shifting up by a few kilohertz. The increased wind speed drives waves on the surface of the water, which has two effects. First, it alters the angle of incidence of raindrops on the water; this reduces the probability that an individual droplet will produce a bubble from 100% at normal incidence to 10% at a deviation of 20° (Ma & Nystuen, 2005). Additionally, a deviation of 20° causes a 30% decrease in the energy emitted by the initial impact (Ma & Nystuen, 2005). This means the dominance of the bubble noise over the impact noise reduces by a factor of 10, making the peak less prominent. Second, as we will discuss later, at high wind speeds, breaking waves (white caps) can also produce bubbles of similar magnitude, which interfere with the sound of rainfall. However, it has been observed that under certain conditions, rainfall can prevent the formation of breaking waves (Leighton, 1994; Wu, 1979; Cavaleri, 2020; Holthuijsen, 2007).

Some studies have noted a secondary rise in the rain spectrum starting at 2–3 kHz and peaking around 5 kHz. This is believed to be a consequence of irregular entrainment of bubbles caused by very large droplets 2.0–3.5 mm in diameter (Serra, 2018; Yang et al., 2015; Pensieri et al., 2015; Taylor et al., 2020; Anagnostou et al., 2008). We had previously dismissed irregular entrainment and the entrainment of large bubbles by assuming all the droplets impacted at terminal velocity and that larger droplets were less common than small ones. However, it appears that when a rainstorm consists of particularly large droplets (>2.0 mm), the frequency of irregular and large entrainment events is significant enough to cause a recognizable spike in the spectrum, possibly as a result of accompanying wave action lowering the impact velocity. This secondary 5 kHz peak, although less conspicuous than the 14–15 kHz peak, may be more useful, as it exists in the part of the spectrum less affected by wind and wave noise (2–10 kHz) (Ma & Nystuen, 2005). Thus, observations of the intensity of the 5 kHz peak can be used for rainfall quantification regardless of wind speeds. Using comparative rain gauge data, Ma and Nystuen (2001) proposed the following equation for calculating the rainfall rate S_{rain} in mm/hr based on the SPL at 5 kHz ($SPL_{5\text{kHZ}}$):

$$10 \log_{10} S_{\text{rain}}/10 = (SPL_{5\text{kHZ}} - 42.4)/15.4. \quad (10.13)$$

Although the exact relationship varies from location to location based on local conditions and ambient noise levels, acoustic inversion of rainfall (with sufficient calibration) is a highly promising technique for use in meteorological and oceanographic research and is becoming increasingly common (Ma & Nystuen, 2005, 2007; Yang et al., 2015; Pensieri et al., 2015; Taylor et al., 2020; Anagnostou et al., 2008; Nystuen et al., 2000; Deane & Stokes, 2002).

In summary, the acoustic signature of rainfall in the marine environment is caused by the entrainment of bubbles, not the impact of the droplets themselves. The rain spectrum is a distinctive peak at 14–15 kHz with a sudden drop-off below 10–12 kHz, caused by regular entrainment, and occasionally a secondary smaller peak at 5 kHz, caused by irregular entrainment when droplets are particularly large. The intensity of these peaks is dictated by the number of raindrops impacting the water per second. As the intensity of the rainfall increases, the peaks become broader and less well-defined. Increasing wind speeds also mute the 14–15 kHz peak by altering the impact angle of droplets and interference from wave noise; however, the 5 kHz peak is less affected by wind and can be used for rainfall quantification.

10.5. ACOUSTICS OF BREAKING WAVES

In the natural marine environment, sufficiently high wind speeds can cause surface gravity waves to break as whitecaps (or white horses) (Leighton, 1994). Unsurprisingly, this process entrains a large number of bubbles that oscillate near the surface, as described by equation 10.5 (Deane & Stokes, 2002; Bass & Hay, 1997; Manasseh et al, 2006; Farmer & Vagle, 1988). Not only do these bubbles have a noticeable effect on the ambient noise of the ocean (via oscillation) (Deane & Stokes, 2002), but they also may affect the passage of other acoustic signals by altering the propagation of sound waves near the sea surface (Deane & Stokes, 2002). First we will discuss waves as acoustic sources before discussing the effect wave-generated bubbles have on the speed of sound. Then we will discuss ambient noise generated by wave action and how this can be related to wind speed. We will not discuss in detail the hydrodynamic controls behind breaking waves, other than to note that in general, strong winds

result in larger breaking waves (which would demand a full chapter) (Leighton, 1994; Deane & Stokes, 2002).

The entrainment of bubbles from wave action is a highly dynamic process (even more so than rainfall), with the exact minutia of bubble generation being poorly understood (Deane & Stokes, 2002). We know, however, from laboratory and field data that distinct bubbles are initially generated during one of two phases: jet entrainment and cavity collapse (Deane & Stokes, 2002).

Jet entrainment begins as soon as the wave starts to break. The crest of the wave overturns and plunges into the wave face, forming a plunging jet with a cavity of air trapped between the two bodies of water. This chaotic collision of the jet generates bubbles, generally between 0.1 and 2.0 mm in radius (2 to 30 kHz) (Leighton, 1994). Additionally, the impact of the jet causes the water to splash and a number of droplets to also entrain bubbles. Toward the end of a breaking wave's life cycle, the air cavity trapped between the wave face and the plunging jet collapses. This forms many bubbles, most of which are between 2.0 and 10.0 mm in radius (0.4 to 2 kHz) (Deane & Stokes, 2002). Given the high density of bubbles, the remnants of the cavity act as a bubble cloud. As discussed earlier, bubbles in a cloud tend to act as coupled oscillators with normal modes of oscillation much lower than that of individual bubbles (Deane & Stokes, 2002; Carey & Bradley, 1985). The cavity-collapse phase is thus responsible for frequencies between 0.1 and 0.5 kHz due to the bubble cloud and higher frequencies up to ~2 kHz from individual oscillations (Deane & Stokes, 2002; Carey & Bradley, 1985). At this time, the plunging jet also forms a shear zone along the wave surface, which encircles the cavity remnants. Some bubbles are pulled through this shear zone, which can cause a bubble to fragment into two or more smaller fragments that once again oscillate although at a higher frequency than their parent bubble (Leighton, 1994; Deane & Stokes, 2002, 2010). For example, a large bubble oscillating at 3.1 kHz may produce two daughters, one at 50 kHz and the other at 32.3 kHz (Deane & Stokes, 2002; Thorpe, 1982). The intensity of the cavity-collapse signature is far greater than that of the jet period (or later shearing); thus, when waves continuously break in the marine environment, the sound of these bubble clouds dominates. Therefore, the acoustic signature of a breaking wave near the surface can most easily be recognized by a low-frequency signal between approximately 0.2 and 2 kHz (Deane & Stokes, 2002; Carey & Bradley, 1985), distinct from that of rain and gas seeps (Bergès et al., 2015; Ma & Nystuen, 2005).

Deane and Stokes (2002) presented the average acoustic signature of 10 cm plunging breakers (Fig. 10.9). Here, one can clearly see the jet period—continuous throughout the breaking of the wave—responsible for the signal above 2 kHz, with the majority of the sound generated below 10 kHz. The cavity-collapse period can also be clearly identified as a quick (~0.3 s) low-frequency burst centered around 0.3 kHz (Deane & Stokes, 2002; Thorpe, 1982). It should be intuitive that the acoustic signature (or rather, the resulting bubble cloud) of a wave is a consequence of its size (and the style of breaking), which is typically a function of wind speed. Thus, by observing the breaking of a wave, one can infer the acoustic signal or vice versa.

Given the energetic and variable nature of breaking waves, it is difficult to predict exactly what happens to the resulting bubbles postproduction. The exception is during Langmuir circulation—the slow, shallow, counter-rotational vortices aligned with wind direction that develop when the wind blows steadily over a body of water—which has been extensively analyzed. After formation, Langmuir circulation can carry wave-generated bubbles up to 10 m below the surface (Monahan & Lu, 1990). In wind speeds >7 m/s, this has been known to result in linear bubble clouds orientated parallel to the wind direction (Leighton, 1994). These *Langmuir bubble clouds* consist of bubbles produced throughout the lifecycle of a wave (jet and cavity-collapse phase) and potentially those entrained by rainfall. Individual bubbles in the cloud naturally shrink due to dissolution and eventually disappear (Liang et al., 2011); however, a high concentration of bubbles may delay this process. A continued supply of freshly generated bubbles can allow the cloud to persist as long as circulation is active. (Leighton, 1994; Liang et al., 2011; Clay & Medwin, 1977) The clouds generally have void fractions between 10^{-4} and 10^{-5}% that are assumed to be uniform in the horizontal plane but fall off exponentially with depth (Leighton, 1994; Farmer & Vagle, 1988; Vagle et al., 1990; Farmer et al., 2001).

As the speed of sound depends on the inertia and stiffness of the material it is passing through, the speed of sound in a bubble cloud (or bubbly liquid) differs from that of pure water. Gas is less dense than water, so sound waves travel more slowly through bubble clouds, becoming slower the larger and more numerous the bubbles are—that is, the larger the void fraction (Garrett et al., 2000; Wang et al., 2016). If there is a distribution of bubble sizes within a cloud, such that $n_n^{gr}(z, R)dR_0$ is the number of bubbles per unit volume at depth z having radii between R_0 and $R_0 + dR_0$, the speed of sound in a cloud c_c is given by (Clay & Medwin, 1977)

$$c_c(z,\omega) = c\left\{1-\left(2\pi c^2\right)\int_{R_0=0}^{\infty}\frac{R_0}{\omega^2}\left(\frac{(\omega_0/\omega)^2-1}{\left\{(\omega_0/\omega)^2-1\right\}^2+d^2}\right)n_n^{gr}(z,R)dR_0\right\}, \tag{10.14}$$

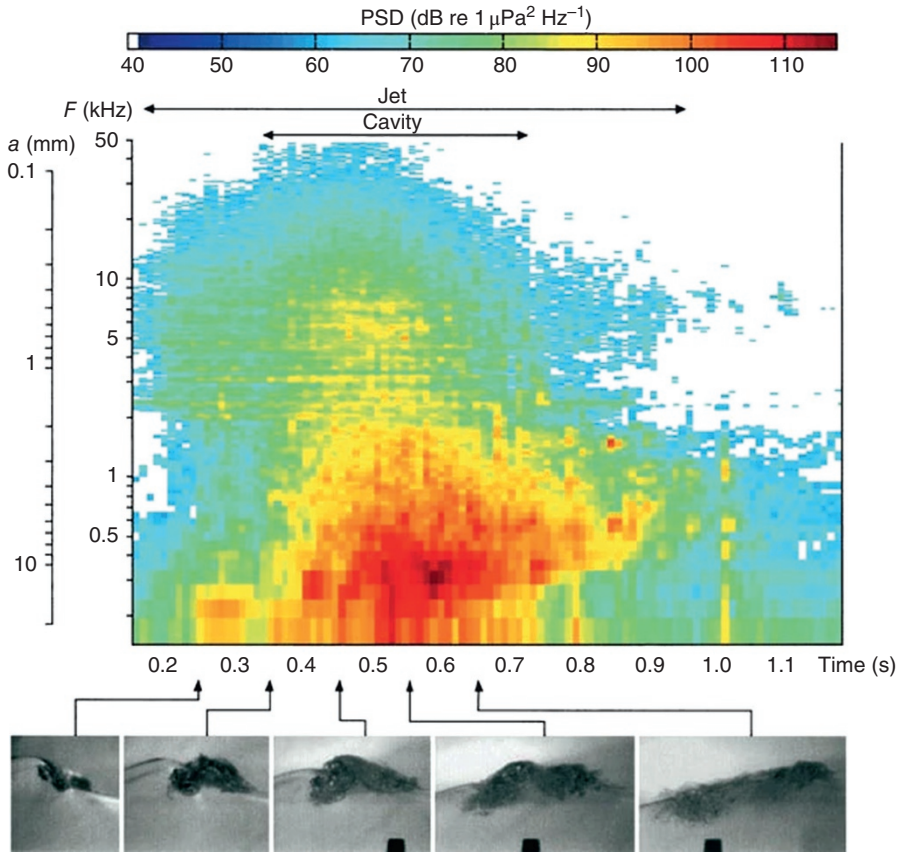

Figure 10.9 Spectrogram of wave noise calculated from an average of 17 breaking events. Note the jet and cavity phases. The color contours represent sound intensity plotted on a decibel scale (the intensity if referenced to 1 $\mu Pa^2/Hz$) versus frequency and time. The log scale labeled *a* on the left-hand side indicates the radius of a bubble resonant at the corresponding frequency of the frequency scale (*F*). The wave noise was measured by a hydrophone mounted in the wave flume beneath the bubble plume. The images plotted below the spectrogram show the sequence of flow features at different times during the acoustic emissions. Deane et al. (2002) / Reproduced from Springer *Nature*.

where d is the dimensionless damping constant for a single bubble, and ω_0 is the resonant circular frequency of the bubble given by $\omega_0 = 2\pi f_0$.

Given the above and the fact that surface-generated bubble clouds tend to decrease in concentration with depth, one can see how the presence of breaking waves can result in an ocean model where sound speed increases noticeably with depth in the upper ~10 m (Leighton, 1994; Knudsen et al., 1948; Wenz, 1962; Farmer & Vagle, 1989; Buckingham, 1991; Zhao et al., 2014). In such a scenario, downward-propagating sound waves tend to turn, due to refraction, bending upward back toward the surface. Similarly, upward-propagating waves also turn, refracting downward. Repeating this cycle can result in the horizontal propagation of sound waves, trapping acoustic energy in the near surface (Deane & Stokes, 2010; Farmer et al., 2001). In terms of wave acoustics, Farmer and Vagle (1989) and Buckingham (1991) both suggested that for a given mode, the signal becomes evanescent (unable to propagate further) below a certain extinction depth. They suggest that the trapping of sound in such a waveguide may influence the ambient acoustic spectra of wave noise and that by observing certain drop-out frequencies, one could infer the bubble-size population generated by breaking waves, although Buckingham argues the loss of signal alone is not sufficient for a full analysis (Farmer & Vagle, 1989; Buckingham, 1991). Unfortunately, the latter appears correct, as despite numerous attempts in the following years, little progress has been made inverting bubble populations from wave acoustics (Garrett et al., 2000; Wang et al., 2016).

Accounting for bubble-cloud effects, Deane and Stokes (2010) presented a model for calculating the underwater noise of a single breaking wave at a distance r with good agreement with experimental observations. Here, assuming wave noise is a superposition of oscillations from generated bubbles, with the creation times of bubbles being uniform and randomly distributed throughout the breaking period, the Power spectrum is given by

$$P(\omega, r) = \int_V \int_{a_{\min}}^{a_{\max}} \lambda(a, r) |\gamma(\omega, a)\alpha(\omega, a)|^2 da dV, \quad (10.15)$$

where $a_{\min}$ and $a_{\max}$ are the minimum and maximum bubble sizes generated, V is the plume volume, $\lambda(a, r)$ is the rate at which bubbles are generated, and $\gamma(\omega, a)$ and $\alpha(\omega, a)$ are the Fourier transforms of the convolution of free-space bubble pulses and Green's function for the medium of propagation, respectively (Deane & Stokes, 2010).

With an understanding of the individual acoustic signal of a breaking wave and how bubble clouds affect the near surface, one might assume that calculating the resulting signal of multiple breaking waves would be straightforward. After all, at a given depth, an observer will record a signal that is the superposition of all the waves breaking above it at any given moment. Given a large enough area and a sufficient number of waves—that is, an ocean—one can assume a constant number of waves are breaking, resulting in a constant ambient noise, as is the case with rainfall. Indeed, if all the waves were identical and occurring in some symmetrical pattern around the recorder, we could attempt to estimate the signal via theoretical calculations. However, this is unrealistic and would be of little practical use; a range of breaking wave sizes and styles will always exist, distributed erratically along the sea surface (Bass & Hay, 1997; Manasseh et al., 2006; Knudsen et al., 1948; Wenz, 1962). Additionally, a detailed understanding of the size distribution of bubbles generated in a breaking wave $\lambda(a, r)$ in equation 10.15 is required, something lacking outside easily replicable waves (Deane & Stokes, 2010).

For simplicity's sake, the seminal work of Knudsen et al. (1948) and Wenz (1962) describing the ambient SPL in the ocean at different wind speeds using field observations, seen in Fig. 10.6, is still relevant (Medwin & Beaky, 1989; Vagle et al., 1990; Zhao et al., 2014). It starts at around 0.20 kHz and rises 3–5 dB re 1 μPa^2/Hz to a peak at approximately 0.5 kHz (consistent with the above discussion) before dropping off slowly, ~25 dB re 1 μPa^2/Hz by 10 kHz, with peak SPLs of 60 and 73 dB re 1 μPa^2/Hz, respectively, for wind speeds of 3.4–5.5 m/s and 17.2–20.7 m/s (Farmer & Vagle, 1988; Vagle et al., 1990; Zhao et al., 2014; Felizardo & Melville., 1995). This does not generally cover strong gales (wind speed >20.8 m/s), as during higher wind speeds, it becomes difficult to identify periods of pure wind noise (i.e., non-rain-contaminated).

Despite the complexity of the task, however, many still wish to be able to calculate the ambient noise of breaking waves: for example, for storm monitoring (Yang et al., 2015; Pensieri et al., 2015; Anagnostou et al., 2008; Zhao et al., 2014; Zhao et al., 2017) or studying ocean atmospheric mixing (Deane & Stokes, 2002; Vagle et al., 2010). The most widespread approach is via WOTAN (Wind Observations Through Ambient Noise) calculations. Here, observations of the ambient noise from breaking waves have been correlated with wind speed through numerous studies to empirically map their relationship (Vagle et al., 1990; Zhao et al., 2014). Originally this work was done to estimate wind speed based on ambient wave noise, but the reverse should also be possible (calculating ambient wave noise based on wind speed).

Using past studies and their data, Vagle et al. (1990) determined that the source sound level at a depth of 1 m from breaking waves was given by

$$SSL_0 = q \log f + G, \quad (10.16)$$

where q is the slope of the logarithmic spectrum of the wind-generated sound, which they find to be equal to –19.0 dB/decade (in good agreement with past estimates (Farmer & Vagle, 1988)). G is a variable function of wind speed. Vagle et al. (1990) determined values for G between set wind speeds, which we note approximately follow $G = 1.3U_{10}+56$ (U_{10} being the wind speed 10 m above water level). Unfortunately, this sound-level equation only holds true for low wind speeds ($U_{10} \leq 15$ m/s) and below a certain critical frequency, $\log f_c = 1.9 - 0.07U_{10}$ (Vagle et al., 2010).

Zhao et al. (2014) expanded on this work by studying typhoons' underwater acoustics using Lagrangian floats. Figure 10.10 displays the spectral content they observed at a range of high wind speeds from a number of floats. They noted that low-frequency sound (<1 kHz) monotonically increased with wind speed, whereas while intermediate and higher frequencies initially increased and then decreased with wind speed. They presented the following empirical equation to calculate the sound pressure level of a given frequency in wind speeds up to 50 m/s (Zhao et al., 2014):

$$SPL = S_{\text{noise}} + S_{10} \frac{\left(U_{10}/10\right)^{n_{lf}}}{1 + \left(U_{10}/f_{\text{peak}}\right)^{n_{hf}}}, \quad (10.17)$$

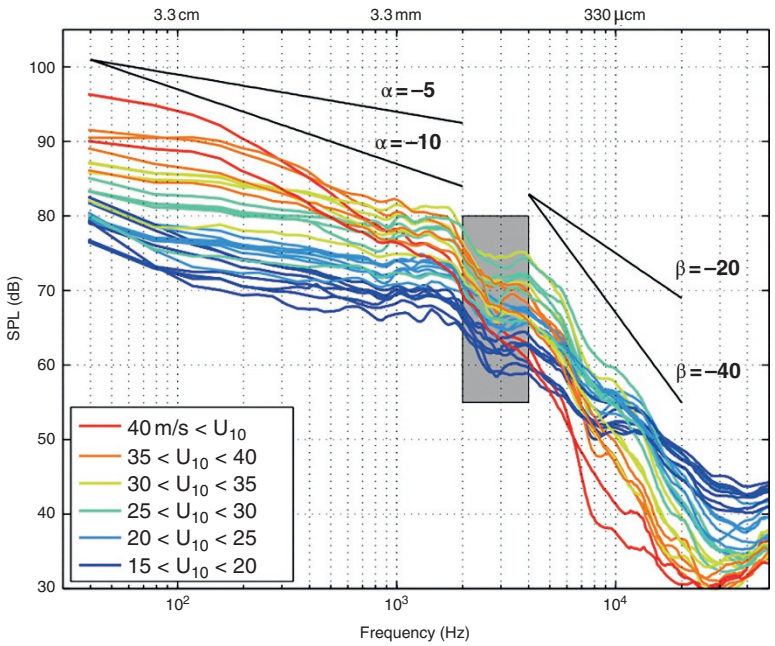

Figure 10.10 Spectrogram of breaking-wave noise at various wind speeds recorded at sea during tropical cyclones. Each curve averages all spectra in 5 m/s wind speed bins from measurements at depth >2 m of a single float; multiple curves of the same color denote observations from multiple floats. The four black lines show representative spectral slopes at low (α) and high (β) frequencies. The gray box shows the transition frequency (2–4 kHz) between the two slope regions. The dip in sound level near 3 kHz may be an instrumental effect. Zhao et al. (2014) / American Meteorological Society.

where S_{noise} is the noise floor, S_{10} is the sound level at 10 m/s wind, f_{peak} controls the wind speed with the sound level maximum, and n_{lf} and n_{hf} are values that control the increasing/decreasing in lower/higher wind conditions. All of these values are a function of the target frequency, although the exact relationship is not fully understood or linear and is determined instead by least-square fitting of observations (Zhao et al., 2014). Consequently, real-time analysis of wind speed via acoustics is still an emerging field. Although highly promising, this approach needs to be tested in multiple environments many more times, especially if the underlying variables are to be better understood (Pensieri et al., 2015; Vagle et al., 1990; Zhao et al., 2014; Cazau et al., 2019; Cazau et al., 2017; Farrell et al., 2016; Cauchy et al., 2018).

It should be apparent from the above that accurately predicting the acoustic signal recorded at a hydrophone as a result of breaking waves at any given wind speed is an exceedingly difficult task, especially in gale-force winds (>17.6 m/s) (Vagle et al., 1990; Zhao et al., 2014), and particularly without some prior observations for calibration. Furthermore, many empirical WOTAN studies are intrinsically flawed for the purpose of calculating noise levels at depth as they only study the effects of wind on specific frequencies. Additionally, without a better understanding of the effect bubble clouds have on the downward propagating of the signal, estimations at depth (>100 m) are highly speculative.

In summary, the acoustic signature of a breaking wave is primarily the result of bubble-cloud generation during the final cavity collapse phase of a wave's life cycle. Although individual bubble frequencies range from 0.4 to 2.0 kHz, the frequency of the bubble cloud itself is typically lower, at 0.1 to 0.5 kHz. The exact frequency spectrum depends on the properties of the wave, which are usually a consequence of wind speed and can be highly variable even under laboratory conditions. Bubbles generated by breaking waves can be pulled down as much as 10 m by Langmuir currents, where they can create steep sound-speed profiles with depth, possibly trapping select acoustic signals. The highly dynamic and unpredictable nature of breaking waves makes predicting ambient noise

from multiple breaking waves difficult, especially in gale-force winds. WOTAN allow for measurements of wind speed via the ambient noise of wave action based on empirical observations but is insufficient for calculating ambient noise at depth. Knudsen curves are still the most commonly used prediction of ambient noise from wave action, with a positively skewed peak at around 0.5 kHz increasing in intensity with wind speed.

10.6. CONCLUSION

Bubbles have subtle yet far-reaching effects on marine acoustics. The initial formation of a bubble triggers simple harmonic motion at a natural frequency known as the Minnaert frequency, which is approximately inversely proportional to the bubble's radius. Thus, by observing the acoustic signature of a bubble, one can determine its size. Although the sound of a single bubble is low energy, the continuous release of multiple bubbles can significantly impact the ambient marine soundscape. To accurately predict the ambient noise produced by a gas seep, rainfall, or breaking waves, one must have a detailed understanding of the size distribution of bubbles being generated. Unfortunately, it is all but impossible to predict the size of bubbles released. However, it is possible to use observations of ambient noise to infer the characteristics of these sources: the flux from a gas seep, the intensity of rainfall, and the wind speed resulting in breaking waves.

FURTHER READING

The following sources are recommended for continuing research in each area introduced in this chapter:

- Bubble physics:
  - Leighton, T. G. (1994). The freely-oscillating bubble. In *The Acoustic Bubble* (pp. 129–286). Elsevier. https://doi.org/10.1016/B978-0-12-441920-9.50008-0
- Subsea gas-seep acoustics:
  - Leighton, T. G., & White, P. R. (2012). Quantification of undersea gas leaks from carbon capture and storage facilities, from pipelines and from methane seeps, by their acoustic emissions. *Proceedings of the Royal Society A: Mathematical, Physical and Engineering Sciences 468*, 485–510.
  - Bergès, B. J. P., Leighton, T. G., & White, P. R. (2015). Passive acoustic quantification of gas fluxes during controlled gas release experiments. *International Journal of Greenhouse Gas Control, 38*, 64–79.
- Rainfall acoustics:
  - Serra, Y. L. (2018). Precipitation measurements from the Tropical Moored Array: a review and look ahead. *Quarterly Journal of the Royal Meteorological Society, 144*, 221–234.
  - Ma, B. B., & Nystuen, J. A. (2005). Passive acoustic detection and measurement of rainfall at sea. *Journal of Atmospheric and Oceanic Technology, 22*, 1225–1248.
  - Pumphrey, H. C., & Crum, L. A. (1990). Free oscillations of near-surface bubbles as a source of the underwater noise of rain. *The Journal of the Acoustical Society of America, 87*, 142–148.
  - Pumphrey, H. C., & Elmore, P. A. The entrainment of bubbles by drop impacts. *Journal of Fluid Mechanics, 220*, 539–567 (1990).
  - Pumphrey, H.C., & Walton, A.J., 1988. Experimental study of the sound emitted by water drops impacting on a water surface. *European Journal of Physics*, *9*, 225–231. https://doi.org/10.1088/0143-0807/9/3/011
- Breaking wave acoustics:
  - Deane, G. B., & Stokes, M. D. (2002). Scale dependence of bubble creation mechanisms in breaking waves. *Nature, 418*, 839–844.
  - Deane, G. B., & Stokes, M. D. (2010). Model calculations of the underwater noise of breaking waves and comparison with experiment. *The Journal of the Acoustical Society of America, 127*, 3394–3410.
  - Zhao, Z., D'Asaro, E. A., & Nystuen, J. A. (2014). The sound of tropical cyclones. *Journal of Physical Oceanography, 44*, 2763–2778.
  - Leighton, T. G. (1994). The freely-oscillating bubble. In *The Acoustic Bubble* (pp. 129–286). Elsevier. https://doi.org/10.1016/B978-0-12-441920-9.50008-0
  - Vagle, S., Large, W. G., & Farmer, D. M. An evaluation of the WOTAN technique of inferring oceanic winds from underwater ambient sound. *Journal of Atmospheric and Oceanic Technology, 7*, 576–595 (1990).

APPENDIX

Minnaert Frequency Derivation

The following is a derivation of the Minnaert equation following Leighton (1994).

We can find the kinetic energy, φ_K, of the water surrounding a bubble by integrating over shells of liquid from the bubble wall to infinity. A shell of radius r and a thickness dr has a mass of $4\pi r^2 \rho dr$ (where ρ is the density of

water), and thus the kinetic energy of the surrounding water is

$$\varphi_K = \int_R^\infty \left(4\pi r^2 \rho\, dr\right) \dot{r}^2. \tag{A1}$$

The mass of liquid flowing in time dt through any spherical surface around the bubble is $4\pi r^2 \dot{r} \rho dt$. Assuming the liquid is incompressible, then by conservation of mass, this general flow can be equated to the flow at the bubble surface, which can be shown to be $\dot{r}/\dot{R} = R^2/r^2$. Substituting this into the above gives

$$\varphi_K = 2\pi R^3 \rho \dot{R}^2 \tag{A2}$$

Kinetic energy is a maximum at the equilibrium position (as with any harmonic oscillator) when $R = R_0$ and $\dot{R} = i\omega_0 R_{\varepsilon 0} e^{i\omega_0 t}$, implying that $\left|\dot{R}\right|^2 = (\omega_0 R_{\varepsilon 0})^2$. Thus, the maximum value of the kinetic energy is

$$\varphi_{\mathrm{KMax}} = \frac{1}{2} m_{\mathrm{RF}}^{\mathrm{rad}} (\omega_0 R_{\varepsilon 0})^2 = 2\pi {R_0}^3 \rho (\omega_0 R_{\varepsilon 0})^2, \tag{A3}$$

where $m_{\mathrm{RF}}^{\mathrm{rad}}$ is the radiation mass of the bubble in the radius-force frame. This mass is the effective inertia of the liquid component of the oscillating system the pulsating bubble represents: that is, $m_{\mathrm{RF}}^{\mathrm{rad}} = 4\pi {R_0}^3 \rho$. It arises from the liquid that is transmitting acoustic waves and is the only inertia considered by the Minnaert derivation.

Through conservation of energy, the maximum kinetic energy φ_{KMax} must equal the maximum internal energy φ_{PMax}, which occurs when $R = R_0 \pm R_{\varepsilon 0}$ and $\dot{R} = 0$. The work done compressing the bubble from equilibrium volume V_0 (at radius R_0) to minimum volume $V_{\min}$ (at radius $R_0 - R_{\varepsilon 0}$) is the integral of $-(p_g - p_0)dV$, where p_g is the gas pressure and p_0 is the hydrostatic liquid pressure outside the bubble:

$$\varphi_{\mathrm{PMax}} = -\int_{V_{\max}}^{V_{\min}} \left(p_g - p_0\right) dV = -\int_{R_0}^{R_0 - R_{\varepsilon 0}} \left(p_g - p_0\right) 4\pi r^2\, dr \tag{A4}$$

Minnaert derived his equation assuming that the gas behaved adiabatically: that is, that there was no heat flow across the bubble wall. This was adapted by the introduction of the polytropic index κ (which takes a value equal to unity when the gas behaves isothermally and equals the ratio of the specific heat of the gas at constant pressure to that at constant volume when the gas behaves adiabatically) (Leighton & Walton, 1987). Assuming the gas behaves polytropically so that $p_g V^\kappa = constant$, then since $R_\varepsilon = R - R_0$, equating the pressure and volume condition at equilibrium to those when the bubble attains minimum volume gives

$$p_g (R_0 + R_\varepsilon)^{3k} = p_0 {R_0}^{3k}. \tag{A5}$$

For small displacements, the binomial expansion of this is

$$p_0 - p_g \approx \frac{3\kappa R_\varepsilon p_0}{R_0}. \tag{A6}$$

Substituting this into the maximum internal energy φ_{PMax} with the use of first-order $R_\varepsilon = R - R_0$ coordinates gives

$$\varphi_{PMax} = \int_0^{R_{\varepsilon 0}} \frac{3\kappa R_\varepsilon p_0}{R_0} 4\pi {R_0}^2\, dR_\varepsilon = 6\pi\kappa p_0 R_0 {R_{\varepsilon 0}}^2. \tag{A7}$$

This allows us to equate the maximum kinetic energy and maximum potential energy:

$$\varphi_{KMax} = 2\pi {R_0}^3 \rho (\omega_0 R_{\varepsilon 0})^2 = 6\pi\kappa p_0 R_0 {R_{\varepsilon 0}}^2 = \varphi_{PMax}, \tag{A8}$$

which can be solved for the resonance circular frequency ω_0:

$$\omega_0 = \frac{1}{R_0}\sqrt{\frac{3\kappa p_0}{\rho}} \tag{A9}$$

Finally, using $\omega_0 = 2\pi f_M$ gives us the Minnaert frequency equation:

$$f_M = \frac{1}{2\pi R_0}\sqrt{\frac{3\kappa p_0}{\rho}}. \tag{A10}$$

SYMBOLOGY

Symbol	Definition
$a_{\min}$	Minimum bubble size generated
$a_{\max}$	Maximum bubble size generated
$B(R_0)$	Bubble-size distribution
c	Speed of sound in water
c_c	Speed of sound through a bubble cloud
d	Dimensionless damping constant for a single bubble $=2\beta/\omega$
D	Initial dipole strength of the bubble
f	Frequency
f_{peak}	Peak frequency
f_M	Minnaert frequency: oscillation frequency of a bubble as predicted by the Minnaert equation
f_0	Natural frequency of a bubble oscillation
G	A variable function of wind speed

Symbol	Definition
h	Distance from the center of the bubble to the surface of the water
I_{Rain}	Intensity of rainfall beneath the surface at a given frequency
ISL_{Rain}	Intensity spectrum level of rainfall beneath the surface at a given frequency
l	Loaded length of spring
l_0	Unloaded length of spring
L_d	Diameter of water droplet
m_{RF}^{rad}	Radiation mass of bubble in radius force frame
n	Mode number
$n(f)$	Number of bubbles entrained per second by rainfall
n_{lf}	A quantity controlling the increasing slope of wave noise in lower wind conditions
n_{hf}	A quantity controlling the decreasing slope of wave noise in higher wind conditions
$n_n^{gr}(z, R)dR_0$	Number of bubbles per unit volume at depth z having a radii between R_0 and $R_0 + dR_0$
N_b	Number of identical bubbles in a bubble cloud
p_g	Gas pressure inside the bubble
p_0	Hydrostatic liquid pressure outside the bubble
p_v	Vapor pressure
$P(\omega, r)$	Power spectrum of a breaking wave
q	Quality factor
Q_w	Slope of the logarithmic spectrum of the wind-generated sound
r	Radial distance
R	Radius of Bubble wall
R_0	Equilibrium radius of bubble
R_ε	Displacement of the bubble wall from equilibrium radius
$R_{\varepsilon 0}$	Maximum displacement of bubble wall from equilibrium radius
$R_{\varepsilon 0i}$	Initial amplitude of displacement of the bubble wall
R_{max}	Maximum radius of bubble
R_{min}	Minimum radius of bubble
S	Column vector containing the measured spectrum $S(\omega_k)$
$S(\omega)$	Power spectral density of a marine gas seep
S_{10}	Sound level at 10 ms^{-1} wind
S_{noise}	Noise floor
S_{rain}	Rainfall rate
SPL	Sound pressure level
SPL_{5kHZ}	Sound pressure level at 5 kHz
SSL_0	Source sound level of breaking waves at a depth of 1m
t	Time
u	Impact Mach number
u_d	Impact speed of water droplet
U_{10}	Wind speed 10 m above water level
V	Volume of bubble plume
V_0	Equilibrium bubble volume
V_{min}	Minimum bubble volume
VF	Void Fraction

Symbol	Definition
z	Depth below sea surface
$\alpha(\omega, a)$	Fourier transform of the Greens function for the medium of propagation, respectively
$\gamma(\omega, a)$	Fourier transform of the convolution of free-space bubble pulses
δ_{tot}	Total damping constant for bubble pulsation at resonance
ε	Displacement from equilibrium
θ	Polar angle, angle between observer and source relative to the z axis
φ_K	Kinetic energy
φ_{KMax}	Maximum kinetic energy
φ_{PMax}	Maximum internal energy
κ	Polytropic index
σ	Surface tension
η	Shear viscosity
ρ	Density of water
ω	Angular frequency $=2\pi f$
ω_0	Angular resonate frequency
$\Psi(n)$	Bubble generation rate (for marine gas seep)

REFERENCES

Ainslie, M. A., & Leighton, T. G. (2011). Review of scattering and extinction cross-sections, damping factors, and resonance frequencies of a spherical gas bubble. *The Journal of the Acoustical Society of America*, *130*(5), 3184–3208.

Algar, C. K., Boudreau, B. P., & Barry, M. A. (2011). Initial rise of bubbles in cohesive sediments by a process of viscoelastic fracture. *Journal of Geophysical Research*, *116*, B04207.

Anagnostou, M. N., Nystuen, J. A., Anagnostou, E. N., Nikolopoulos, E. I., & Amitai, E. (2008). Evaluation of underwater rainfall measurements during the ionian sea rainfall experiment. *IEEE Transactions on Geoscience and Remote Sensing*, *46*, 2936–2946.

Ashokan, M., Latha, G., & Ramesh, R. (2015). Analysis of shallow water ambient noise due to rain and derivation of rain parameters. *Applied Acoustics*, *88*, 114–122.

Bass, S. J., & Hay, A. E. (1997). Ambient noise in the natural surf zone: wave-breaking frequencies. *IEEE Journal of Oceanic Engineering*, *22*, 411–424.

Bergès, B. J. P., Leighton, T. G., & White, P. R. (2015). Passive acoustic quantification of gas fluxes during controlled gas release experiments. *International Journal of Greenhouse Gas Control*, *38*, 64–79.

Black, P. G., Proni, J. R., Wilkerson, J. C., & Samsury, C. E. (1997). Oceanic rainfall detection and classification in tropical and subtropical mesoscale convective systems using underwater acoustic methods. *Monthly Weather Review*, *125*, 2014–2042.

Boles, J. R., Clark, J. F., Leifer, I., & Washburn, L. (2001). Temporal variation in natural methane seep rate due to tides, Coal Oil Point area, California. *Journal of Geophysical Research: Oceans*, *106*, 27077–27086.

Böttner, C., Berndt, C., Reinardy, B. T. I., Geersen, J., Karstens, J., Bull, J. M., et al. (2019). Pockmarks in the Witch Ground Basin, Central North Sea. *Geochemistry, Geophysics, Geosystems*, *20*, 1698–1719.

Boudreau, B. P. (2012). The physics of bubbles in surficial, soft, cohesive sediments. *Marine and Petroleum Geology*, *38*(1), 1–18.

Boudreau, B. P., Algar, C. K., Johnson, B. D., Croudace, I., Reed, A., Furukawa, Y., et al. (2005). Bubble growth and rise in soft sediments. *Geology*, *33*(6), 517.

Buckingham, M. J. (1991). On acoustic transmission in ocean-surface waveguides. *Philosophical Transactions: Physical Sciences and Engineering*, *335*, 513–555.

Carey, W. M., & Bradley, M. P. (1985). Low-frequency ocean surface noise sources. *The Journal of the Acoustical Society of America*, *78*, S1–S2.

Cauchy, P., Heywood, K. J., Merchant, N. D., Queste, B. Y., & Testor, P. (2018). Wind speed measured from underwater gliders using passive acoustics. *Journal of Atmospheric and Oceanic Technology*, *35*, 2305–2321.

Cavaleri, L. (2020). Rain, wave breaking and spray. In *Recent advances in the study of oceanic whitecaps* (pp. 65–75). Springer International Publishing. https://doi.org/10.1007/978-3-030-36371-0_5

Cavaleri, L., & Bertotti, L. (2018). Rain on generative seas. *Geophysical Research Letters*, *45*, 7049–7056.

Cazau, D., Bonnel, J., & Baumgartner, M. (2019). Wind speed estimation using acoustic underwater glider in a near-shore marine environment. *IEEE Transactions on Geoscience and Remote Sensing*, *57*, 2097–2106.

Cazau, D., Bonnel, J., Jouma'a, J., le Bras, Y., & Guinet, C. (2017). Measuring the marine soundscape of the Indian Ocean with southern elephant seals used as acoustic gliders of opportunity. *Journal of Atmospheric and Oceanic Technology*, *34*, 207–223.

Chen, L., Trinh, V., Yang, W., & Mohanangam, K. (2016). Prediction of bubble generation based on acoustic emission. *Acoustics Australia*, *44*, 325–331.

Clay, C. S., & Medwin, H. (1977). Acoustical oceanography: principles and applications. *Journal of the Marine Biological Association of the United Kingdom*, *58*, 543–543.

Coughlan, M., Roy, S., O'Sullivan, C., Clements, A., O'Toole, R., & Plets, R. (2021). Geological settings and controls of fluid migration and associated seafloor seepage features in the north Irish Sea. *Marine and Petroleum Geology*, *123*, 104762.

Czerski, H., & Deane, G. B. (2010). Contributions to the acoustic excitation of bubbles released from a nozzle. *The Journal of the Acoustical Society of America*, *128*(5), 2625–2634.

Deane, G. B., & Stokes, M. D. (2002). Scale dependence of bubble creation mechanisms in breaking waves. *Nature*, *418*, 839–844.

Deane, G. B., & Stokes, M. D. (2010). Model calculations of the underwater noise of breaking waves and comparison with experiment. *The Journal of the Acoustical Society of America*, *127*, 3394–3410.

Esposito, A., Giordano, G., & Anzidei, M. (2006). The 2002–2003 submarine gas eruption at Panarea volcano (Aeolian Islands, Italy): volcanology of the seafloor and implications for the hazard scenario. *Marine Geology*, *227*, 119–134.

Farmer, D. M., & Vagle, S. (1988). On the determination of breaking surface wave distributions using ambient sound. *Journal of Geophysical Research*, *93*, 3591.

Farmer, D. M., & Vagle, S. (1989). Waveguide propagation of ambient sound in the ocean-surface bubble layer. *The Journal of the Acoustical Society of America*, *86*, 1897–1908.

Farmer, D. M., Deane, G. B., & Vagle, S. (2001). The influence of bubble clouds on acoustic propagation in the surf zone. *IEEE Journal of Oceanic Engineering*, *26*, 113–124.

Farrell, W. E., Berger, J., Bidlot, J.-R., Dzieciuch, M., Munk, W., Stephen, R. A., & Worcester, P. F. (2016). Wind sea behind a cold front and deep ocean acoustics. *Journal of Physical Oceanography*, *46*, 1705–1716.

Felizardo, F. C., & Melville, W. K. (1995). Correlations between ambient noise and the ocean surface wave field. *Journal of Physical Oceanography*, *25*, 513–532.

Garrett, C., Li, M., & Farmer, D. (2000). The connection between bubble size spectra and energy dissipation rates in the upper ocean. *Journal of Physical Oceanography*, *30*, 2163–2171.

Greene, C. A., & Wilson, P. S. (2012). Laboratory investigation of a passive acoustic method for measurement of underwater gas seep ebullition. *The Journal of the Acoustical Society of America*, *131*, EL61–EL66.

Holthuijsen, L. H. (2007). *Waves in oceanic and coastal waters*. Cambridge University Press. https://doi.org/10.1017/CBO9780511618536

Hovland, M. (2002). On the self-sealing nature of marine seeps. *Continental Shelf Research*, *22*, 2387–2394.

Jain, A. K., & Juanes, R. (2009). Preferential mode of gas invasion in sediments: grain-scale mechanistic model of coupled multiphase fluid flow and sediment mechanics. *Journal of Geophysical Research*, *114*, B08101.

Johnson, B. D., Barry, M. A., Boudreau, B. P., Jumars, P. A., & Dorgan, K. M. (2012). In situ tensile fracture toughness of surficial cohesive marine sediments. *Geo-Marine Letters*, *32*(1), 39–48.

Johnson, B. D., Boudreau, B. P., Gardiner, B. S., & Maass, R. (2002). Mechanical response of sediments to bubble growth. *Marine Geology*, *187*(3-4), 247–363.

Judd, A. G. (2003). The global importance and context of methane escape from the seabed. *Geo-Marine Letters*, *23*(2), 147–154.

Klaucke, I., Weinrebe, W., Petersen, C. J., & Bowden, D. (2010). Temporal variability of gas seeps offshore New Zealand: multi-frequency geoacoustic imaging of the Wairarapa area, Hikurangi margin. *Marine Geology*, *272*, 49–58.

Knittel, K., & Boetius, A. (2009). Anaerobic oxidation of methane: progress with an unknown process. *Annual Review of Microbiology*, *63*, 311–334.

Knudsen, V. O., Alford, R. S., & Emling, L. W. (1948). Underwater ambient noise. *Marine Research*, *7*.

Leifer, I. (2015). Seabed bubble flux estimation by calibrated video survey for a large blowout seep in the North Sea. *Marine and Petroleum Geology*, *68*, 743–752.

Leifer, I., & Patro, R. K. (2002). The bubble mechanism for methane transport from the shallow sea bed to the surface:

a review and sensitivity study. *Continental Shelf Research*, *22*, 2409–2428.

Leighton, T. G. (1988). The frequency analysis of transients. *European Journal of Physics*, *9*, 69–70.

Leighton, T. G. (1994). The freely-oscillating bubble. In *The acoustic bubble* (pp. 129–286). Elsevier. https://doi.org/10.1016/B978-0-12-441920-9.50008-0

Leighton, T. G. (2004). From seas to surgeries, from babbling brooks to baby scans: the acoustics of gas bubbles in liquids. *International Journal of Modern Physics B*, *18*(18), 3267–3314.

Leighton, T. G., & Walton, A. J. (1987). An experimental study of the sound emitted from gas bubbles in a liquid. *European Journal of Physics*, *8*, 98–104.

Leighton, T. G., & White, P. R. (2012). Quantification of undersea gas leaks from carbon capture and storage facilities, from pipelines and from methane seeps, by their acoustic emissions. *Proceedings of the Royal Society A: Mathematical, Physical and Engineering Sciences*, *468*(2140), 485–510.

Leighton, T. G., K.J., F., & Field, J.E. (1991). Acoustic and photographic studies of injected bubbles. *European Journal of Physics*, *12*, 77–85.

Leighton, T. G., White, P. R., & Schneider, M. F. (1998). The detection and dimension of bubble entrainment and comminution. *The Journal of the Acoustical Society of America*, *103*(4), 1825–1835.

Li, J., Roche, B., Bull, J. M., White, P. R., Davis, J. W., Deponte, M., Gordini, E., & Cotterle, D. (2020a). Passive acoustic monitoring of a natural CO2 seep site – implications for carbon capture and storage. *International Journal of Greenhouse Gas Control*, *93*, 102899.

Li, J., Roche, B., Bull, J. M., White, P. R., Leighton, T. G., Provenzano, G., et al. (2020b). Broadband acoustic inversion for gas flux quantification—application to a methane plume at Scanner pockmark, Central North Sea. *Journal of Geophysical Research: Oceans*, *125*.

Li, J., White, P. R., Roche, B., Bull, J. M., Leighton, T. G., Davis, J. W., & Fone, J. W. (2021). Acoustic and optical determination of bubble size disruptions - quantification of undersea gas emissions. *International Journal of Greenhouse Gas Control.*

Liang, J.-H., McWilliams, J. C., Sullivan, P. P., & Baschek, B. (2011). Modeling bubbles and dissolved gases in the ocean. *Journal of Geophysical Research*, *116*, C03015.

Longuet-Higgins, M. S., Kerman, B. R., & Lunde, K. (1991). The release of air bubbles from an underwater nozzle. *Journal of Fluid Mechanics*, *230*, 365–390.

Lu, N. Q., Prosperetti, A., & Yoon, S. W. (1990). Underwater noise emissions from bubble clouds. *IEEE Journal of Oceanic Engineering*, *15*(3), 275–281.

Ma, B. B., & Nystuen, J. A. (2005). Passive acoustic detection and measurement of rainfall at sea. *Journal of Atmospheric and Oceanic Technology*, *22*, 1225–1248.

Ma, B. B., & Nystuen, J. A. (2007). Detection of rainfall events using underwater passive aquatic sensors and air–sea temperature changes in the tropical Pacific Ocean. *Monthly Weather Review*, *135*, 3599–3612.

Maksimov, A. O., Burov, B. A., Salomatin, A. S., & Chernykh, D. V. (2016). Sounds of undersea gas leaks. In *Underwater acoustics and ocean dynamics* (pp. 107–116). Springer Singapore. https://doi.org/10.1007/978-981-10-2422-1_15

Manasseh, R., Babanin, A. V., Forbes, C., Rickards, K., Bobevski, I., & Ooi, A. (2006). Passive acoustic determination of wave-breaking events and their severity across the spectrum. *Journal of Atmospheric and Oceanic Technology*, *23* (4), 599–618.

McGinnis, D. F., Greinert, J., Artemov, Y., Beaubien, S. E., & Wüest, A. (2006). Fate of rising methane bubbles in stratified waters: how much methane reaches the atmosphere? *Journal of Geophysical Research*, *111*, C09007.

Medwin, H., & Beaky, M. M. (1989). Bubble sources of the Knudsen sea noise spectra. *The Journal of the Acoustical Society of America*, *86*(3), 1124–1130.

Medwin, H., Kurgan, A., & Nystuen, J. A. (1990). Impact and bubble sound from raindrops at normal and oblique incidence. *The Journal of the Acoustical Society of America*, *88*, 413–418.

Minnaert, M. (1933). On musical air-bubbles and the sounds of running water. *The London, Edinburgh, and Dublin Philosophical Magazine and Journal of Science*, *16*, 235–248.

Monahan, E. C., & Lu, M. (1990). Acoustically relevant bubble assemblages and their dependence on meteorological parameters. *IEEE Journal of Oceanic Engineering*, *15*, 340–349.

Muyakshin, S. I., & Sauter, E. (2010). The hydroacoustic method for the quantification of the gas flux from a submersed bubble plume. *Oceanology*, *50*, 995–1001.

Nystuen, J. A. (1986). Rainfall measurements using underwater ambient noise. *The Journal of the Acoustical Society of America*, *79*, 972–982.

Nystuen, J. A. (2001). Listening to raindrops from underwater: an acoustic disdrometer. *Journal of Atmospheric and Oceanic Technology*, *18*, 1640–1657.

Nystuen, J. A., & Selsor, H. D. (1997). Weather classification using passive acoustic drifters. *Journal of Atmospheric and Oceanic Technology*, *14*, 656–666.

Nystuen, J. A., Amitai, E., Anagnostou, E. N., & Anagnostou, M. N. (2008). Spatial averaging of oceanic rainfall variability using underwater sound: Ionian sea rainfall experiment 2004. *The Journal of the Acoustical Society of America*, *123*, 1952–1962.

Nystuen, J. A., Anagnostou, M. N., Anagnostou, E. N., & Papadopoulos, A. (2015). Monitoring Greek seas using passive underwater acoustics. *Journal of Atmospheric and Oceanic Technology*, *32*, 334–349.

Nystuen, J. A., McPhaden, M. J., & Freitag, H. P. (2000). Surface measurements of precipitation from an ocean mooring: the underwater acoustic log from the South China Sea. *Journal of Applied Meteorology*, *39*, 2182–2197.

Ostrovsky, I., McGinnis, D. F., Lapidus, L., & Eckert, W. (2008). Quantifying gas ebullition with echosounder: The role of methane transport by bubbles in a medium-sized lake. *Limnology and Oceanography: Methods*, *6*, 105–118.

Pensieri, S., Bozzano, R., Nystuen, J., Anagnostou, E., Anagnostou, M., & Bechini, R. (2015). Underwater acoustic measurements to estimate wind and rainfall in the Mediterranean Sea. *Advances in Meteorology*, *2015*, 1–18.

Phelps, A. D., Ramble, D. G., & Leighton, T. G. (1997). The use of a combination frequency technique to measure the surf

zone bubble population. *The Journal of the Acoustical Society of America*, *101*(4), 1981–1989.

Pumphrey, H. C. (1989). *Sources of ambient noise in the ocean: an experimental investigation* (PhD thesis). Mississippi University.

Pumphrey, H. C., & Crum, L. A. (1990). Free oscillations of near-surface bubbles as a source of the underwater noise of rain. *The Journal of the Acoustical Society of America*, *87* (1), 142–148.

Pumphrey, H. C., & Elmore, P. A. (1990). The entrainment of bubbles by drop impacts. *Journal of Fluid Mechanics*, *220*, 539–567.

Pumphrey, H. C., & Walton, A. J. (1988). Experimental study of the sound emitted by water drops impacting on a water surface. *European Journal of Physics*, *9*, 225–231.

Riedel, M., Scherwath, M., Römer, M., Veloso, M., Heesemann, M., & Spence, G. D. (2018). Distributed natural gas venting offshore along the Cascadia margin. *Nature Communications*, *9*, 3264.

Roche, B., Bull, J. M., Marin-Moreno, H., Leighton, T. G., Suarez, I. F., Tholen, M., et al. (2020). Time-lapse imaging of CO2 migration within near-surface sediment during a controlled sub-seabed release experiment. *International Journal of Greenhouse Gas Control*, *109*, 103363.

Roche, B., Li, J., White, P., Bull, J., Davis, J., Deponte, M., et al. (2019). Validating passive acoustic methods for gas flux quantification, offshore Panarea, Mediterranean Sea. *The Journal of the Acoustical Society of America*, *146*, 2965–2965.

Römer, M., Riedel, M., Scherwath, M., Heesemann, M., & Spence, G. D. (2016). Tidally controlled gas bubble emissions: A comprehensive study using long-term monitoring data from the NEPTUNE cabled observatory offshore Vancouver Island. *Geochemistry, Geophysics, Geosystems*, *17*, 3797–3814.

Scandella, B. P., Pillsbury, L., Weber, T., Ruppel, C., Hemond, H. F., & Juanes, R. (2016). Ephemerality of discrete methane vents in lake sediments. *Geophysical Research Letters*, *43*, 4374–4381.

Scrimger, J. A., Evans, D. J., McBean, G. A., Farmer, D. M., & Kerman, B. R. (1987). Underwater noise due to rain, hail, and snow. *The Journal of the Acoustical Society of America*, *81*, 79–86.

Serra, Y. L. (2018). Precipitation measurements from the Tropical Moored Array: a review and look ahead. *Quarterly Journal of the Royal Meteorological Society*, *144*, 221–234.

Strasberg, M. (1953). The pulsation frequency of nonspherical gas bubbles in liquids. *The Journal of the Acoustical Society of America*, *25*(3), 536–537.

Suess, E. (2014). Marine cold seeps and their manifestations: Geological control, biogeochemical criteria and environmental conditions. *International Journal of Earth Sciences*, *103*, 1889–1916.

Sultan, N., Plaza-Faverola, A., Vadakkepuliyambatta, S., Buenz, S., & Knies, J. (2020). Impact of tides and sea-level on deep-sea Arctic methane emissions. *Nature Communications*, *11*, 5087.

Taylor, W. O., Anagnostou, M. N., Cerrai, D., & Anagnostou, E. N. (2020). Machine learning methods to approximate rainfall and wind from acoustic underwater measurements. *IEEE Transactions on Geoscience and Remote Sensing*, *1–12*. https://doi.org/10.1109/TGRS.2020.3007557

Thorpe, S. A. (1982). On the clouds of bubbles formed by breaking wind-waves in deep water, and their role in air--sea gas transfer. *Philosophical Transactions of the Royal Society of London. Series A, Mathematical and Physical Sciences*, *304*, 155–210.

Vagle, S., Large, W. G., & Farmer, D. M. (1990). An evaluation of the WOTAN technique of inferring oceanic winds from underwater ambient sound. *Journal of Atmospheric and Oceanic Technology*, *7*, 576–595.

Vagle, S., McNeil, C., & Steiner, N. (2010). Upper ocean bubble measurements from the NE Pacific and estimates of their role in air-sea gas transfer of the weakly soluble gases nitrogen and oxygen. *Journal of Geophysical Research*, *115*, C12054.

Vazquez, A., Manasseh, R., & Chicharro, R. (2015). Can acoustic emissions be used to size bubbles seeping from a sediment bed? *Chemical Engineering Science*, *131*, 187–196.

Walton, A. J., Gunn, M. G., & Reynolds, G. T. (2005). The quality factor of oscillating bubbles as an indication of gas content with particular reference to methane. *IEEE Journal of Oceanic Engineering*, *30*(4), 924–926.

Wang, D. W., Wijesekera, H. W., Jarosz, E., Teague, W. J., & Pegau, W. S. (2016). Turbulent diffusivity under high winds from acoustic measurements of bubbles. *Journal of Physical Oceanography*, *46*, 1593–1613.

Wenz, G. M. (1962). Acoustic ambient noise in the ocean: Spectra and sources. *The Journal of the Acoustical Society of Tommy America*, *34*, 1936–1956.

Wiggins, S. M., Leifer, I., Linke, P., & Hildebrand, J. A. (2015). Long-term acoustic monitoring at North Sea well site 22/4b. *Marine and Petroleum Geology*, *68*, 776–788.

Wu, J. (1979). Oceanic whitecaps and sea state. *Journal of Physical Oceanography*, *9*, 1064–1068.

Yang, J., Riser, S., Nystuen, J., Asher, W., & Jessup, A. (2015). Regional rainfall measurements using the passive aquatic listener during the SPURS field campaign. *Oceanography*, *28*, 124–133.

Zhao, B., Qiao, F., Cavaleri, L., Wang, G., Bertotti, L., and Liu, L. (2017). Sensitivity of typhoon modeling to surface waves and rainfall. *Journal of Geophysical Research: Oceans*, *122*, 1702–1723.

Zhao, Z., D'Asaro, E. A., & Nystuen, J. A. (2014). The sound of tropical cyclones. *Journal of Physical Oceanography*, *44*, 2763–2778.